

University of Groningen

Revised Extinctions and Radii for 1.5 Million Stars Observed by APOGEE, GALAH, and RAVE

Yu, Jie; Khanna, Shourya; Themessl, Nathalie; Hekker, Saskia; Dréau, Guillaume; Gizon, Laurent; Bi, Shaolan

Published in:
Astrophysical Journal, Supplement Series

DOI:
[10.3847/1538-4365/acabc8](https://doi.org/10.3847/1538-4365/acabc8)

IMPORTANT NOTE: You are advised to consult the publisher's version (publisher's PDF) if you wish to cite from it. Please check the document version below.

Document Version
Publisher's PDF, also known as Version of record

Publication date:
2023

[Link to publication in University of Groningen/UMCG research database](#)

Citation for published version (APA):

Yu, J., Khanna, S., Themessl, N., Hekker, S., Dréau, G., Gizon, L., & Bi, S. (2023). Revised Extinctions and Radii for 1.5 Million Stars Observed by APOGEE, GALAH, and RAVE. *Astrophysical Journal, Supplement Series*, 264(2), Article 41. <https://doi.org/10.3847/1538-4365/acabc8>

Copyright

Other than for strictly personal use, it is not permitted to download or to forward/distribute the text or part of it without the consent of the author(s) and/or copyright holder(s), unless the work is under an open content license (like Creative Commons).

The publication may also be distributed here under the terms of Article 25fa of the Dutch Copyright Act, indicated by the "Taverne" license. More information can be found on the University of Groningen website: <https://www.rug.nl/library/open-access/self-archiving-pure/taverne-amendment>.

Take-down policy

If you believe that this document breaches copyright please contact us providing details, and we will remove access to the work immediately and investigate your claim.

Downloaded from the University of Groningen/UMCG research database (Pure): <http://www.rug.nl/research/portal>. For technical reasons the number of authors shown on this cover page is limited to 10 maximum.



Revised Extinctions and Radii for 1.5 Million Stars Observed by APOGEE, GALAH, and RAVE

Jie Yu¹, Shourya Khanna^{2,3}, Nathalie Themessl⁴, Saskia Hekker^{4,5}, Guillaume Dréau⁶, Laurent Gizon^{1,7,8}, and Shaolan Bi⁹

¹ Max-Planck-Institut für Sonnensystemforschung, Justus-von-Liebig-Weg 3, D-37077 Göttingen, Germany; yujie@mps.mpg.de

² Kapteyn Astronomical Institute, University of Groningen, Groningen, 9700 AV, The Netherlands

³ INAF—Osservatorio Astrofisico di Torino, via Osservatorio 20, I-10025 Pino Torinese (TO), Italy

⁴ Landessternwarte Königstuhl (LSW), Heidelberg University, Königstuhl 12, D-69117 Heidelberg, Germany

⁵ Heidelberg Institute for Theoretical Studies (HITS) gGmbH, Schloss-Wolfsbrunnengasse 35, D-69118 Heidelberg, Germany

⁶ LESIA, Observatoire de Paris, PSL Research University, CNRS, Université Pierre et Marie Curie, Université Paris Diderot, F-92195 Meudon, France

⁷ Institut für Astrophysik, Georg-August-Universität Göttingen, Friedrich-Hund-Platz 1, D-37077 Göttingen, Germany

⁸ Center for Space Science, NYUAD Institute, New York University Abu Dhabi, PO Box 129188, Abu Dhabi, UAE

⁹ Department of Astronomy, Beijing Normal University, Beijing 100875, People's Republic of China

Received 2022 May 29; revised 2022 December 5; accepted 2022 December 6; published 2023 February 1

Abstract

Asteroseismology has become widely accepted as a benchmark for accurate and precise fundamental stellar properties. It can therefore be used to validate and calibrate stellar parameters derived from other approaches. Meanwhile, one can leverage large-volume surveys in photometry, spectroscopy, and astrometry to infer stellar parameters over a wide range of evolutionary stages, independently of asteroseismology. Our pipeline, SEDEX (<https://github.com/Jieyu126/SEDEX>), compares the spectral energy distribution predicted by the MARCS and BOSZ model spectra with 32 photometric bandpasses, combining data from nine major, large-volume photometric surveys. We restrict the analysis to targets with available spectroscopy from the APOGEE, GALAH, and RAVE surveys to lift the temperature–extinction degeneracy. The cross-survey atmospheric parameter and uncertainty estimates are homogenized with artificial neural networks. Validation of our results with CHARA interferometry, Hubble Space Telescope CALSPEC spectrophotometry, and asteroseismology shows that we achieve high precision and accuracy. We present a catalog of improved interstellar extinction ($\sigma_{A_V} \simeq 0.14$ mag) and stellar radii ($\sigma_R/R \simeq 7.4\%$) for ~ 1.5 million stars in the low-to-high-extinction ($A_V \lesssim 6$ mag) fields observed by the spectroscopic surveys. We derive global extinctions for 184 Gaia DR2 open clusters and confirm the differential extinction in NGC 6791 and NGC 6819, which have been subject to extensive asteroseismic analysis. Furthermore, we report 36,854 double-lined spectroscopic main-sequence binary candidates. This catalog will be valuable for providing constraints on detailed modeling of stars and for constructing 3D dust maps of the Kepler field, the TESS Continuous Viewing Zones, and the PLATO long-duration observation fields.

Unified Astronomy Thesaurus concepts: [Interstellar extinction \(841\)](#); [Stellar properties \(1624\)](#); [Astronomical techniques \(1684\)](#); [AB photometry \(2168\)](#); [Photometry \(1234\)](#); [Spectral energy distribution \(2129\)](#)

Supporting material: machine-readable tables

1. Introduction

Over the past decade, asteroseismology has significantly advanced several fields of astrophysics. One of the main reasons is that asteroseismology can provide accurate and precise fundamental parameters, such as stellar radius, surface gravity, and age, as well as distance and extinction (see reviews by Chaplin & Miglio 2013; Hekker & Christensen-Dalsgaard 2017). However, this technique is limited, as it requires long, high-precision, short-cadence light curves, which have so far been available only for a limited number of CoRoT (~ 3000 ; de Assis Peralta et al. 2018), Kepler ($\sim 16,000$; Yu et al. 2018), and K2 ($\sim 19,000$; Zinn et al. 2022) stars. The ongoing TESS mission (Ricker et al. 2015) has expanded the asteroseismic star sample by one order of magnitude but is restricted to nearby stars ($\sim 158,000$, with a median distance of 800 pc; Hon et al. 2021).

In the current era of large-volume photometric, spectroscopic, and astrometric surveys, one can exploit these complementary data sets to derive stellar parameters over various evolutionary stages, using a method independent of asteroseismology (e.g., Huber et al. 2017; Mints & Hekker 2017, 2018; Anders et al. 2022). One method to combine all these complementary data sets is to perform spectral energy distribution (SED) fitting, which is used in this work. This method involves matching the observed multiple broadband photometry with that predicted from model stellar spectra, to derive stellar parameters, such as bolometric flux and extinction. By combining these parameters with parallax, one can estimate stellar radius and luminosity. Recent examples of such implementation include studies for determining stellar parameters for Hipparcos and Tycho stars (McDonald et al. 2012, 2017), subgiants in the TESS Southern Continuous Viewing Zone (CVZ; Godoy-Rivera et al. 2021), and dwarfs in general (Vines & Jenkins 2022).

It is worth noting that SED fitting does not depend independently on effective temperature (T_{eff}) and extinction; we refer to such variables as degenerate variables (e.g.,



Original content from this work may be used under the terms of the [Creative Commons Attribution 4.0 licence](#). Any further distribution of this work must maintain attribution to the author(s) and the title of the work, journal citation and DOI.

Bailer-Jones 2011; Andrae et al. 2018). The studies mentioned above either assume zero extinction (McDonald et al. 2012, 2017) or use a typical extinction estimate for the entire sample (Godoy-Rivera et al. 2021). These assumptions are legitimate for particular stellar samples, e.g., nearby stars, but have to be modified to study stars associated with a range of extinctions. One approach is to infer extinctions using a priori known T_{eff} , for example, from spectroscopy with zero-point calibration if necessary. In the past decade, large spectroscopic surveys, such as APOGEE (Abdurro'uf & Aerts 2022), GALAH (Buder et al. 2021), and RAVE (Steinmetz et al. 2020a), have provided precise estimates of T_{eff} , which in turn now allow us to derive precise extinction values.

The SED fitting method offers unique advantages in deriving stellar parameters. First, it is independent of stellar evolutionary models. In comparison, traditional isochrone fitting methods rely heavily on evolutionary models that can introduce substantial systematics (Tayar et al. 2022). There have been persistent discrepancies between models and observations in terms of the determination of stellar parameters for late K- and M-type stars (Kraus et al. 2011; Feiden & Chaboyer 2012; Spada et al. 2013; Mann et al. 2015; Rabus et al. 2019). SED fitting has proven to be a robust method in this spectral-type regime and has served to develop precise empirical relations to estimate radii and masses (Mann et al. 2015). Parameter degeneracy, however, prevents us from fully characterizing stars and any orbiting exoplanets, even with asteroseismology (Cunha et al. 2007). For example, helium fraction, mass, and radius are strongly coupled when using asteroseismic measurements alone (Lebreton & Goupil 2014; Silva Aguirre et al. 2017). Combining luminosities estimated from SED fitting with oscillation frequencies enables us to mitigate the degeneracy issue. Second, SED fitting methods leverage multiple bandpasses of photometry whenever available, thus being robust to photometry outliers (e.g., due to stellar flares). This leads to improvements compared with the so-called direct method that combines parallaxes with single-band infrared photometry, bolometric corrections,¹⁰ and reddening maps (e.g., Huber et al. 2017; Berger et al. 2018; Hardegree-Ullman et al. 2020).

Asteroseismology is widely accepted as a benchmark to provide high-precision stellar ages. This method generally demands precise global seismic parameters, i.e., the frequency of maximum power (ν_{max}) and large frequency separation ($\Delta\nu$), which can be measured from high-precision space-based photometric time series, such as from CoRoT and Kepler. The ongoing TESS mission is expected to provide global seismic parameters for an unprecedented number of sources. However, while it supersedes the sky coverage of its predecessors by scanning the whole sky, the majority of the targets from the first 2 yr were observed for only 27 days. This short duration, in conjunction with lower photometric precision compared with Kepler, leads to a lower frequency resolution, hampering $\Delta\nu$ measurements for most solar-like oscillators. Thus, with TESS data (Hon et al. 2021; Stello et al. 2022), only ν_{max} can be measured at large. Interestingly, Stello et al. (2022) found that an alternative set of stellar observables (T_{eff} , ν_{max} , and radius R , i.e., without $\Delta\nu$) can be used to provide comparable and robust estimates of mass (random uncertainty,

12%) and thus age (37%). Radii derived from SED fitting methods can improve the current precision of stellar ages, vital for understanding the formation and evolution of our Galaxy (e.g., Silva Aguirre et al. 2018; Miglio et al. 2021) and for accurately dating accretion events such as the Gaia–Enceladus merger with the Milky Way (e.g., Chaplin et al. 2020; Borre et al. 2022).

Extinctions derived from SED fitting methods are valuable, e.g., for determining the global extinctions of open clusters. Gaia astrometry and photometry have allowed the homogeneous characterization of 2017 open clusters down to $G = 18$, including the determination of memberships (Cantat-Gaudin et al. 2020). Many of these cluster members have been observed by the APOGEE (Donor et al. 2020) and GALAH (Spina et al. 2021) surveys. The extinction estimates of these individual spectroscopic targets allow us to precisely determine the global extinctions of the open clusters. Meanwhile, the extinction estimates of individual targets are also critical for constructing 3D dust maps for the TESS CVZs,¹¹ as well as the Kepler (Borucki et al. 2010), K2 (Howell et al. 2014), and PLATO (Rauer et al. 2014) fields. Many of the stars in these fields are targets for searching for exoplanets. For planets in the stellar habitable zones, stellar (and therefore planetary) radius estimates are particularly important (Heller et al. 2022). Given that asteroseismology is not generally viable for K and M dwarfs (Huber et al. 2019), Gaia parallaxes and extinctions from 3D dust maps will enable us to obtain stellar radii, which are required for characterizing transiting exoplanets.

In this work, we exploit our SED EXplorer (SEDEX) pipeline to estimate interstellar extinction and stellar radius from combined spectroscopic, photometric, and astrometric data and validate the estimates with CHARA interferometry (ten Brummelaar et al. 2005), Hubble Space Telescope (HST) flux standards (Bohlin et al. 2014), and asteroseismology (Aerts et al. 2010; Basu & Chaplin 2017). We focus on the stars observed by APOGEE, GALAH, and RAVE, given that their spectroscopic T_{eff} values are valuable for lifting the temperature–extinction degeneracy. Our SED fitting method makes use of 32 broad bands of nine large-volume photometry databases (see Table 2), exceeding previous related works (e.g., Berger et al. 2018; Berger et al. 2020; Queiroz et al. 2020; Steinmetz et al. 2020a).

2. Data and Methodology

2.1. Target Selection

Our targets were selected from three large-volume, high-resolution spectroscopic campaigns, i.e., APOGEE (spectral resolution $\sim 22,500$; Wilson et al. 2019; Abdurro'uf & Aerts 2022), GALAH (spectral resolution $\sim 28,000$; De Silva et al. 2015; Buder et al. 2021), and RAVE (spectral resolution ~ 7500 ; Steinmetz et al. 2020a, 2020b). APOGEE has largely observed fields north of the Galactic plane, whereas GALAH and RAVE cover the southern sky. APOGEE predominantly targets red giants, aiming at tracing low Galactic latitudes owing to the near-infrared nature of the survey, while GALAH and RAVE include both dwarfs and giants but essentially omit low Galactic latitudes according to their survey designs, to minimize contamination of unresolved multiple

¹⁰ Both SED fitting and bolometric correction tables are based on model spectra, filter transmission curves, and flux density zero-points of individual filters.

¹¹ The CVZs center the south and north ecliptic poles and span regions with a radius of 12° , i.e., 452 deg^2 . The TESS light curves with a baseline of nearly 1 yr are available for performing asteroseismic analysis, among others.

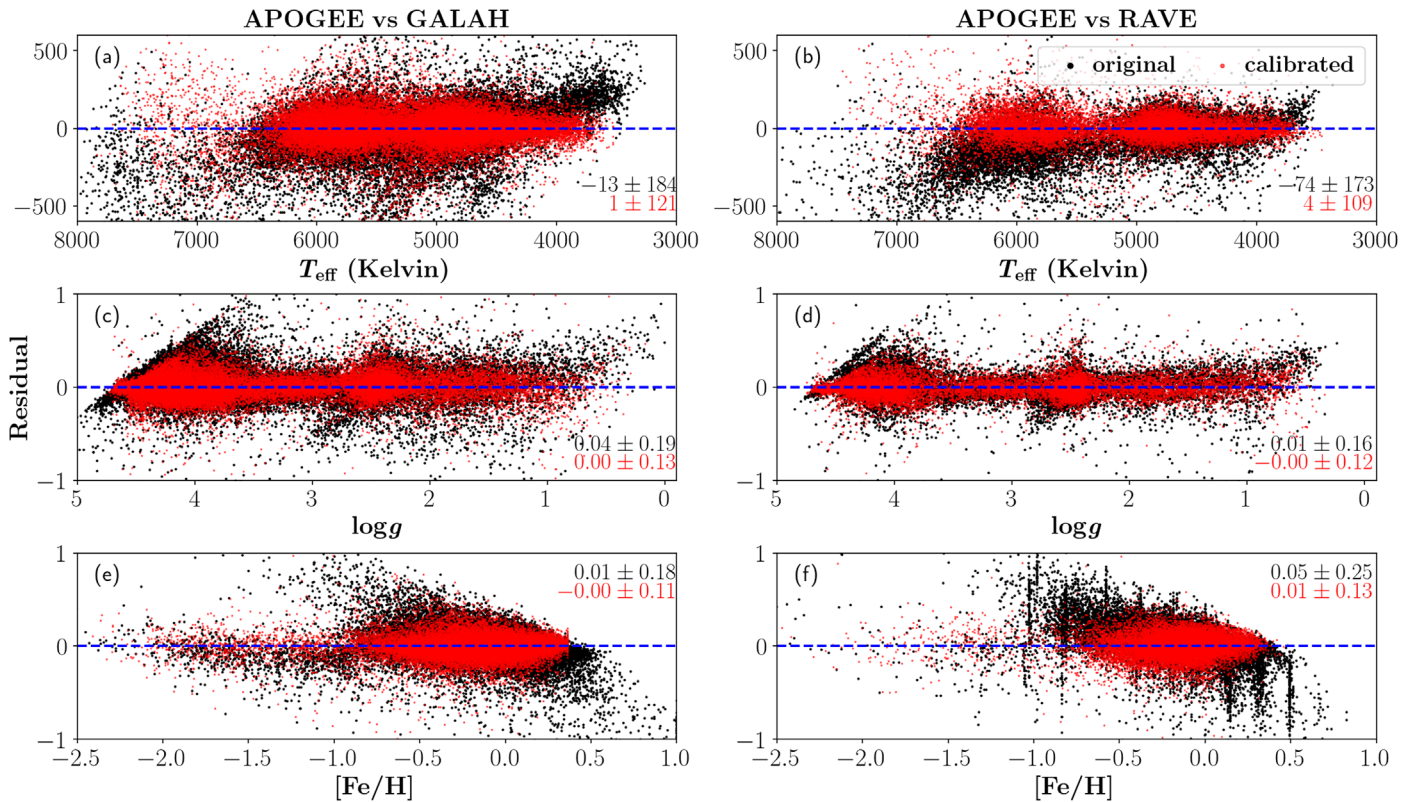


Figure 1. Comparison of the T_{eff} (top row), $\log g$ (middle row), and $[\text{Fe}/\text{H}]$ (bottom row) values of APOGEE DR17 with those of GALAH DR3 (black, left columns) and with those of RAVE DR6 (black, right columns). The red points are similar to the black points, except that the T_{eff} , $\log g$, and $[\text{Fe}/\text{H}]$ estimates in the GALAH and RAVE catalogs are calibrated to match the APOGEE scales (see Section 2.2). The ordinates (residuals) are defined in the sense of APOGEE minus GALAH or APOGEE minus RAVE, whereas the abscissas correspond to GALAH or RAVE. The horizontal lines indicate perfect consistency. The mean offset and standard deviation of the residuals are shown in each panel, with the colors having the same meaning as those of the data points.

sources in a single fiber. APOGEE probes the distant regions of the Galaxy, with a median distance of ~ 1.4 kpc, while GALAH and RAVE target stars that are largely nearby, with a median distance of ~ 800 pc, as revealed by the Gaia parallax-based distances (Bailer-Jones et al. 2021). Thanks to the differences in the spatial distribution and distance, APOGEE naturally probes the high-extinction space, while GALAH and RAVE explore low-extinction regions.

APOGEE DR17 contains 657,135 unique targets (Abdurro’uf & Aerts 2022), from which we selected 616,483 stars whose T_{eff} and $\log g$ estimates are provided, the `STAR_BAD` flag is unset, and Gaia EDR3 source IDs are not NaN or duplicated. GALAH DR3 contains 588,571 stars (Buder et al. 2021), from which we selected 573,593 unique stars, again, by requiring the availability of their T_{eff} and $\log g$ estimates and unique Gaia EDR3 source IDs. RAVE DR6 provides stellar parameters for 451,783 unique stars (Steinmetz et al. 2020a). We focused on its BD sample of 405,059 unique stars with unique Gaia DR3 source IDs. This BD sample is a subset of the RAVE DR6 database that fulfills the basic quality criterion `algo_conv_madera` $\neq 1$ and uses Gaia DR2 distances for deriving stellar atmospheric parameters with the `BDASP` pipeline (for more details, see Section 6 of Steinmetz et al. 2020a).

The entire sample selected above was further filtered by demanding that at least five photometric bands were available for our SED fitting (see Section 2.3 for input photometry). Thus, the combined sample consists of 1,586,926 entries, among which 610,602 stars are included in APOGEE DR17, 572,702 in GALAH DR3, and 403,622 in RAVE DR6. There

are 38,493 stars in common between APOGEE and GALAH, 16,499 between APOGEE and RAVE, and 30,794 between GALAH and RAVE.

2.2. Homogenizing Cross-survey Atmospheric Parameters

The overlapping stars between the three surveys allow us to homogenize their atmospheric parameters. The differences between the cross-survey atmospheric parameter values are shown in Figure 1. Substantial offsets in T_{eff} are visible at low (~ 3800 K) and high T_{eff} (~ 7000 K) values between APOGEE and GALAH and at high T_{eff} (~ 7000 K) values between APOGEE and RAVE (panels (a) and (b)). There is good agreement in $\log g$ between APOGEE and GALAH and between APOGEE and RAVE (panels (c) and (d)). Significant systematic trends are shown in $[\text{Fe}/\text{H}]$, where the $[\text{Fe}/\text{H}]$ residuals between APOGEE and GALAH and between APOGEE and RAVE exhibit linear trends (black points, panels (e) and (f)). Moreover, vertical stripes are present in RAVE $[\text{Fe}/\text{H}]$ (panel (f)). According to Steinmetz et al. (2020a), these stripes occur in stars with low signal-to-noise ratio spectra, which leads to poorer fits. This can be seen in their Figures 8, 9, and 10.

We attempted to minimize the parameter offsets by calibrating the T_{eff} , $\log g$, and $[\text{Fe}/\text{H}]$ estimates of GALAH and RAVE to match those of APOGEE. For this, we used multilayer perceptrons (MLPs; Haykin 1994), a supplement of feedforward neural networks where the data flow in the forward direction from input to output layer. MLPs as a widely recognized algorithm of artificial neural networks are highly

effective to learn nonlinear relations in tabular data. The applications of MLPs for regression can be found in D’Isanto & Polsterer (2018), Ting et al. (2018), and Recio-Blanco et al. (2022), for example. After exploring different network structures, we found that the optimal architecture consists of one input layer of 10 neurons for taking features, three hidden layers with the numbers of neurons decreasing from 32 to 16 to 8, and one output layer for predicting the parameter to be calibrated. We adopted the rectified linear unit (ReLU) as the activation function and the mean squared error as the loss function.

Our 10 input features are T_{eff} , $\log g$, $[\text{Fe}/\text{H}]$, Gaia EDR3 and Two Micron All Sky Survey (2MASS) photometry (G^{12} , G_{BP} , G_{RP} , H , K ; Cutri et al. 2003; Riello et al. 2021), and Gaia EDR3 parallaxes (Lindegren et al. 2021). Our labels are the parameter that we intend to calibrate. For example, for calibrating the GALAH T_{eff} scale to that of APOGEE, the features include T_{eff} , $\log g$, and $[\text{Fe}/\text{H}]$ in GALAH DR3, and the labels are APOGEE T_{eff} values. Similarly, for calibrating the RAVE $[\text{Fe}/\text{H}]$ scale to that of APOGEE, the features include T_{eff} , $\log g$, and $[\text{Fe}/\text{H}]$ in RAVE DR6, and the labels are APOGEE $[\text{Fe}/\text{H}]$ values. We trained six MLPs separately (three MLPs for calibrating GALAH parameters and three for RAVE).

A comparison of our calibrated GALAH and RAVE parameters with those of APOGEE is shown in Figure 1 (red points). The calibrated GALAH and RAVE T_{eff} values are now more consistent with APOGEE, where both the bias and scatter are reduced (see the numbers in panels (a) and (b)). The most significant improvement is in $[\text{Fe}/\text{H}]$, where the linear trends in the residuals are removed. Furthermore, the vertical stripes are modified.

We also updated the heterogeneous uncertainties of T_{eff} , $\log g$, and $[\text{Fe}/\text{H}]$ for the three surveys. Specifically, we first calculated the standard deviation $\sigma_{T_{\text{eff}},AG}$ of the residuals between the APOGEE T_{eff} values and the calibrated GALAH T_{eff} estimates ($\sigma_{T_{\text{eff}},AG} = 121$ K, as given in Figure 1(a)). Similarly, we computed $\sigma_{T_{\text{eff}},AR}$ between APOGEE and RAVE and $\sigma_{T_{\text{eff}},GR}$ between GALAH and RAVE. To determine the typical uncertainties for APOGEE ($\sigma_{T_{\text{eff}},A}$), GALAH ($\sigma_{T_{\text{eff}},G}$), and RAVE ($\sigma_{T_{\text{eff}},R}$), we assume that the three data sets are independent. Thus, we obtain

$$\sigma_{T_{\text{eff}},AG}^2 = \sigma_{T_{\text{eff}},A}^2 + \sigma_{T_{\text{eff}},G}^2 \quad (1)$$

$$\sigma_{T_{\text{eff}},AR}^2 = \sigma_{T_{\text{eff}},A}^2 + \sigma_{T_{\text{eff}},R}^2 \quad (2)$$

$$\sigma_{T_{\text{eff}},GR}^2 = \sigma_{T_{\text{eff}},G}^2 + \sigma_{T_{\text{eff}},R}^2 \quad (3)$$

Solving these three linear equations yields $\sigma_{T_{\text{eff}},A}$, $\sigma_{T_{\text{eff}},G}$, and $\sigma_{T_{\text{eff}},R}$. Finally, we rescaled the T_{eff} uncertainties of each survey by multiplying a factor to ensure that the median value of the rescaled T_{eff} uncertainties is equal to $\sigma_{T_{\text{eff}},A}$ for APOGEE, $\sigma_{T_{\text{eff}},G}$ for GALAH, and $\sigma_{T_{\text{eff}},R}$ for RAVE. We updated $\log g$ and $[\text{Fe}/\text{H}]$ uncertainties for each survey using the same scheme.

The distributions of the original and rescaled parameter uncertainties are shown in Figure 2, and their median uncertainties are given in Table 1. After the scaling, RAVE stars have the most precise T_{eff} and $\log g$ estimates, while APOGEE stars have larger uncertainties. Note that since the

rescaled uncertainties consist of the uncertainties introduced from the calibration process, they do not necessarily represent the intrinsic uncertainties of each survey. We added a T_{eff} error floor of 2.4% in quadrature to the rescaled T_{eff} uncertainties to account for the zero-point uncertainty of spectroscopic T_{eff} estimates (Tayar et al. 2022).¹³ Thus, the systematic 2.4% uncertainties dominate the T_{eff} error budget. The homogeneous stellar atmospheric parameters and their rescaled uncertainties (including the 2.4% systematic T_{eff} uncertainties) were subsequently used for our SED analysis.

2.3. Input Photometry

Observed SEDs were constructed from 32 bandpasses of nine photometric databases, with the following photometric systems when available: Gaia DR3 (Riello et al. 2021), Pan-STARRS DR1 (Chambers et al. 2016), APASS DR9 (Henden et al. 2016), Tycho2 (Høg et al. 2000), Hipparcos (van Leeuwen 2007), SkyMapper DR2 (Onken et al. 2019), Sloan Digital Sky Survey (SDSS) DR13 (Alam et al. 2015), 2MASS (Cutri et al. 2003), and ALLWISE (Cutri et al. 2014). These data sets collectively span a broad range in wavelength, from the optical through the infrared. Generally, the surveys provide measurements averaged over multipoint photometry, such as Gaia photometry. The use of average measurements helps to reduce the scatter due to stellar variability. We discarded ALLWISE photometry in the W3 and W4 bands because of potential biases of their zero-point calibration (see Yu et al. 2021), large photometric uncertainties, and possible contamination by warm interstellar dust (Davenport et al. 2014). We combined the various photometric and spectroscopic data sets, based on their Gaia EDR3 source IDs. For the photometry, these are provided by Gaia (Marrese et al. 2019), while the spectroscopic surveys provide their internal cross-match to Gaia.

We added uncertainty floors in quadrature to the formal magnitude uncertainties of individual photometric catalogs: 0.02 mag for Gaia, Hipparcos, Tycho2, and 2MASS; 0.03 mag for ALLWISE; and 0.06 mag for SDSS, Pan-STARRS, APASS, and SkyMapper (see also Eastman et al. 2019; Godoy-Rivera et al. 2021). We consider this step necessary. First, the SED fitting would otherwise be exclusively controlled by Gaia photometry and less sensitive to the other photometric measurements because of the very small formal uncertainties in Gaia photometry. Second, higher weights should be assigned to Gaia, Hipparcos, Tycho2, 2MASS, and ALLWISE photometry, due to their superior photometric precision for our sample. Lastly, adding uncertainty floors mitigates potential problems associated with the not-well-understood photometric zero-points. These are known to introduce additional uncertainties of up to 1%–2% for ground-based photometry, compared with space-based spectrophotometry from HST/STIS (Bohlin et al. 2014). In case formal uncertainties are unavailable, the uncertainty floors were adopted but inflated by a factor of three.

To account for potential photometric outliers (e.g., due to flares or photometric saturation), we fitted a blackbody distribution to each observed SED, assuming zero extinction. This step was performed iteratively to detect and remove one outlier photometric measurement at each iteration, until none of the flux densities deviated by more than 30% from the best-

¹² G -band photometry used in this work was corrected following the formulae presented in Riello et al. (2021) and implemented with the code listed in their Appendix.

¹³ The 2.4% T_{eff} uncertainty floor is not included in the rescaled errors reported in Table 1.

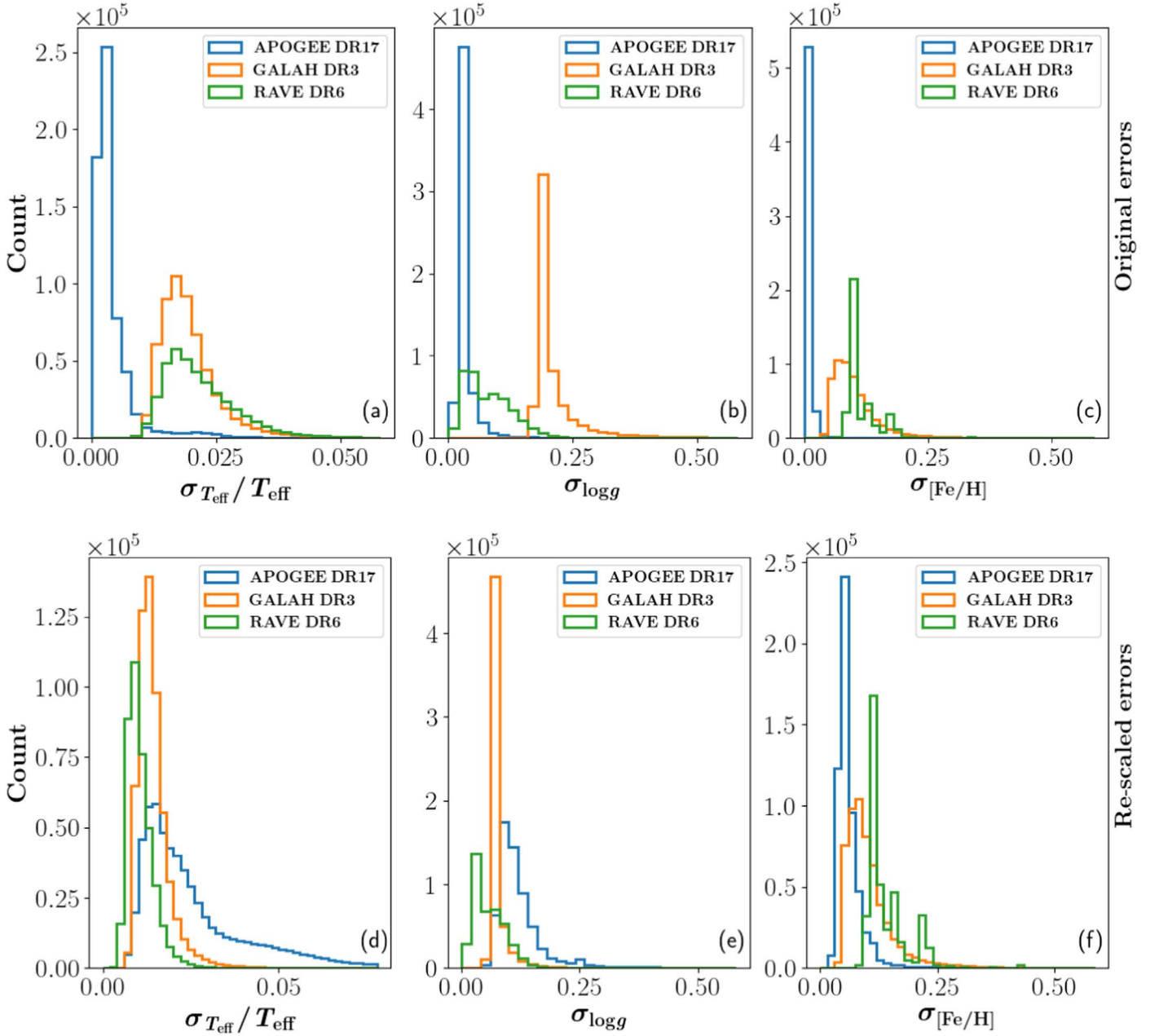


Figure 2. Top: histograms of the heterogeneous uncertainties of T_{eff} (left), $\log g$ (middle), and $[\text{Fe}/\text{H}]$ (right) of APOGEE DR17 (blue), GALAH DR3 (orange), and RAVE DR6 (green). Bottom: similar to the top panels, but now for the rescaled uncertainties that contain the calibration uncertainties and the intrinsic uncertainties (see Section 2.2).

Table 1

Atmospheric Parameter Uncertainties of APOGEE DR17, GALAH DR3, and RAVE DR6

Survey	Rescaled			Original		
	$\sigma_{T_{\text{eff}}}$	$\sigma_{\log g}$	$\sigma_{[\text{Fe}/\text{H}]}$	$\sigma_{T_{\text{eff}}}$	$\sigma_{\log g}$	$\sigma_{[\text{Fe}/\text{H}]}$
APOGEE	99	0.11	0.05	12	0.03	0.008
GALAH	70	0.06	0.09	96	0.19	0.088
RAVE	47	0.05	0.12	97	0.07	0.095

Note. The median T_{eff} , $\log g$, and $[\text{Fe}/\text{H}]$ uncertainties of the individual catalogs before (original) and after (rescaled) the cross-survey scaling (see Section 2.2). Note that the original cross-survey uncertainties are heterogeneous owing to different definitions, while the rescaled uncertainties consist of the calibration and intrinsic uncertainties.

fitting blackbody spectrum. This homogeneous method applied to heterogeneous photometry is preferable over filtering data with a complex combination of photometric quality flags. During this step, magnitudes were converted to flux densities using the absolute calibration of the flux densities of the individual filters listed in Table 2. Next, we computed model flux densities calculated from stellar spectral libraries.

2.4. Model Spectra

Several stellar spectral libraries have been developed for analyzing observed spectra, such as ATLAS (Kurucz 1979), MARCS (Gustafsson et al. 2008), PHOENIX (Husser et al. 2013), and BOSZ (Bohlin et al. 2017), among others. While all

Table 2
Photometric System Parameters

Photometric System	Filter	Mag System	FTC	λ_p (Å)	$\bar{f}_{0,\lambda}$ ($\text{erg s}^{-1} \text{cm}^{-2} \text{Å}^{-1}$)	$\bar{f}_{0,\nu}$ (Jy)	References	m_0 (mag)	References
(1)	(2)	(3)	(4)	(5)	(6)	(7)	(8)	(9)	(10)
Hipparcos	H_P	Vega	λT	5586	3.296E-9	...	1	0	1
Tycho2	B_T	Vega	λT	4220	6.798E-9	...	1	0	1
	V_T	Vega	λT	5350	4.029E-9	...	1	0	1
Gaia EDR3	G_{BP}	Vega	T	5109.7	4.110E-9	...	2	0	2
	G	Vega	T	6217.6	2.536E-9	...	2	0	2
	G_{RP}	Vega	T	7769.1	1.299E-9	...	2	0	2
APASS	B	Vega	λT	4368.4	6.459E-9	...	1	0	1
	V	Vega	λT	5486.2	3.735E-9	...	1	0	1
	g	AB	T	4702.5	...	3631	3	0.003	8
	r	AB	T	6175.6	...	3631	3	-0.006	8
	i	AB	T	7490.0	...	3631	3	-0.016	8
SDSS	u	AB	T	3556.5	...	3631	3	0.037	8
	g	AB	T	4702.5	...	3631	3	-0.010	8
	r	AB	T	6175.6	...	3631	3	0.003	8
	i	AB	T	7490.0	...	3631	3	-0.006	8
	z	AB	T	8946.7	...	3631	3	-0.016	8
Pan-STARRS	g	AB	λT	4814.1	...	3631	4	0	4
	r	AB	λT	6174.3	...	3631	4	0	4
	i	AB	λT	7515.8	...	3631	4	0	4
	z	AB	λT	8663.6	...	3631	4	0	4
	y	AB	λT	9616.9	...	3631	4	0	4
SkyMapper	u	AB	T	3493.36	...	3631	5	0	5
	v	AB	T	3835.93	...	3631	5	0	5
	g	AB	T	5075.19	...	3631	5	0	5
	r	AB	T	6138.44	...	3631	5	0	5
	i	AB	T	7767.98	...	3631	5	0	5
2MASS	J	Vega	λT	12350	3.129E-10	...	6	-0.018	8
	H	Vega	λT	16620	1.133E-10	...	6	0.035	8
	K_S	Vega	λT	21590	4.283E-11	...	6	-0.014	8
ALLWISE	W1	Vega	λT	33526	8.179E-12	...	7	0	7
	W2	Vega	λT	46028	2.415E-12	...	7	0	7
	W3	Vega	λT	115608	6.515E-14	...	7	0	7
	W4	Vega	λT	220883	5.090E-15	...	7	0	7

Note. Column (4) indicates whether each filter transmission curve (FTC) from the original source has been multiplied by λ . Pivot wavelengths, λ_p , given in Column (5), are calculated from the adopted FTCs when they are unavailable from the literature. Since the zero-point flux density values ($\bar{f}_{0,\lambda}$) for the Gaia system are not available from the literature, we calculated them using the Vega spectrum, `alpha_lyr_mod_002.fits`. This spectrum is adopted from the CALSPEC Calibration Database and rescaled to set the flux equal to $f_{550} = 3.62286 \times 10^{-11} \text{ W m}^{-2} \text{ nm}^{-1}$ at wavelength $\lambda = 550.0 \text{ nm}$, which is assumed to be the flux of an unreddened A0V star with $V = 0$ (see also Riello et al. 2021). The references of the FTCs and zero-points ($\bar{f}_{0,\nu}$ and m_0) are given in Columns (8) and (10), respectively. (1) Mann & von Braun 2015; (2) Riello et al. 2021; (3) SDSS website at <http://classic.sdss.org/dr7/instruments/imager/index.html#filters>; (4) Tonry et al. 2012; (5) Bessell et al. 2011; (6) Cohen et al. 2003; (7) Jarrett et al. 2011; (8) Casagrande & VandenBerg 2014.

these models have been widely used in the literature for SED fitting, we chose MARCS in this work for consistency, because this library was adopted for spectrum analyses to determine stellar parameters and chemical abundances by APOGEE (Jonsson et al. 2020), GALAH (Buder et al. 2021), and RAVE (Steinmetz et al. 2020a). We refer the reader to Gustafsson et al. (2008) and the website <https://marcs.astro.uu.se/> for details on MARCS. We note that the maximum wavelength of the spectra in MARCS is $20 \mu\text{m}$, which leads to missing flux when calculating bolometric flux for late-type stars. For this reason, we extrapolated MARCS spectra in logarithmic scale with a cubic polynomial, out to $30 \mu\text{m}$ (Yu et al. 2021).

Given that APOGEE DR17 contains numerous B- and A-type stars and the maximum T_{eff} is 8000 K in the MARCS grid, we adopted the BOSZ library for modeling hotter main-sequence (MS) stars ($T_{\text{eff}} > 8000 \text{ K}$), complementing the MARCS library for modeling cooler stars ($T_{\text{eff}} \leq 8000 \text{ K}$). We note that there is a negligible systematic difference (sub-1%) in the derived radii with the two libraries at this T_{eff} boundary.

To compute the model flux density, we convolve each filter transmission curve (see the references given in Table 2) with MARCS model spectra. All the transmission curves, which are in coarse wavelength intervals, have been interpolated to the

higher model wavelength resolution ($\lambda/\Delta\lambda = 20,000$) in order not to skip any line features (Bessell & Murphy 2012).

2.5. General Fitting

The first step of the fitting process was to search for the best-fitting spectral model without spectral model interpolation. For each star, we began by seeking the MARCS models whose metallicities were closest to the observed one, adopted from the same reference as T_{eff} and $\log g$ (Section 2.1). When observed metallicity estimates are unavailable, solar metallicity was assumed. From these models we chose the models with the four closest grid T_{eff} values with respect to the observed T_{eff} and further picked the models with the four closest grid $\log g$ values compared with the observed $\log g$. This led to a maximum of 16 models, if available, in the $T_{\text{eff}}-\log g$ plane, bracketing the observed values. The best-fitting model was the one with the minimum reduced χ^2 in flux density. To avoid numerical overflow issues in the minimization step, the flux densities and their uncertainties were converted to a logarithmic scale.

The second step was to use the best-fitting model to further remove photometric outliers of the observed SED prepared in Section 2.3 in an iterative way. This procedure is similar to the initial cleaning step introduced in Section 2.3 to refine the input photometry, except that here we fitted SEDs rather than a blackbody. To automatically remove photometric outliers of an observed SED, we calculated the relative difference between the observed and the best-fitting model flux densities and rejected the measurements if they were greater than a threshold. This procedure was repeated until either no more outliers were found or the measurements were too sparse to guarantee a reliable fitting. For the relative difference, we adopted a threshold of 10% and a number of valid photometric measurements no less than 5. Only the fits passing these criteria were retained for the subsequent analysis.

The third step was to estimate stellar parameters and their uncertainties by fitting the pruned SEDs with interpolated models in a Bayesian approach. First, we linearly interpolated the preselected 16 models to obtain the flux densities in logarithmic scale in the 32 bandpasses, with a grid resolution of 5 K in T_{eff} and 0.25 dex in $\log g$. Then, we used normal priors for T_{eff} and $\log g$, which are centered at observed values with the standard deviations equal to observed uncertainties. Our fitting model is

$$F_{\lambda,\text{obs}} = (R/d)^2 10^{-0.4\beta(\lambda)A_V} \times F_{\lambda,\text{mod}}(T_{\text{eff}}, \log g, [\text{Fe}/\text{H}]), \quad (4)$$

where $F_{\lambda,\text{obs}}$ and $F_{\lambda,\text{mod}}$ are the observed and model flux densities, respectively, R is stellar radius, d is heliocentric distance, $\beta(\lambda)$ is an extinction law as a function of wavelength, and A_V is extinction in V . Our likelihood function was assumed to be Gaussian and was optimized with the Levenberg–Marquardt optimization algorithm. Finally, we fitted a Gaussian to each posterior and used its mean and standard deviation to estimate a parameter (e.g., extinction) and its uncertainty, respectively. We refer the reader to Yu et al. (2021) for examples of SED fits.

We note that extinction is a direct output of our pipeline. Bolometric flux is calculated by integrating the best-fitting spectrum, and luminosity is derived by combining bolometric flux and distance. Radius is computed from luminosity and input T_{eff} , and angular radius is inferred from radius and

distance. We adopted photogeometric distances from Bailer-Jones et al. (2021) whenever available and their geometric distances otherwise. The uncertainties in extinction and bolometric flux are estimated from the standard derivations of the Gaussians fitted to the posteriors. The uncertainties in luminosity, radius, and angular radius are obtained via error propagation.

Our SED fitting barely depends on the choice of the following general extinction laws as long as we are using $R(V) = 3.1$ (adopted in our work): CCM89 (Cardelli et al. 1989), O94 (O’Donnell 1994), F99 (Fitzpatrick 1999), F04 (Fitzpatrick 2004), M14 (Maiz Apellaniz et al. 2014), G16 (Gordon et al. 2016, reducing to the F99 model with $f_A = 1.0$), and F19 (Fitzpatrick et al. 2019). We tested the difference between these models by running the fitting for a sample of ~ 7000 asteroseismic targets, including dwarfs and giants (Serenelli et al. 2017; Pinsonneault et al. 2018), and found that the systematic differences in radius and extinction are within the formal uncertainties. This is because the extinction model differences are only significant in the near-infrared. For example, A_λ/A_V can be different by $\sim 10\%$ for 2MASS K_S band. However, except for very cool stars ($T_{\text{eff}} < 3300$ K), the infrared flux does not significantly contribute to the SED, making the extinction laws essentially indistinguishable. For this reason, we adopted the F19 model for our final analysis.

Our fitting allows for a negative extinction estimate for each interpolated model. This accounts for the fact that extinction is coupled with effective temperature, which can be biased by several hundred kelvin. We removed stars with A_V uncertainties not compatible with being positive at 2σ . Allowing for negative extinction thus enables us to analyze low-extinction stars. Our final catalog consists of 1,566,810 entries, among which 1,484,987 are unique stars. The numbers of these entries from APOGEE DR17, GALAH DR3, and RAVE DR6 are 593,374, 571,358, and 402,078, respectively. The homogeneously calibrated atmospheric parameter estimates, their rescaled uncertainties, and the derived parameter values are given in Table 4.

3. Validation

3.1. CHARA Interferometry

We compiled a sample of 180 dwarfs and giants that have been observed by the CHARA interferometer (Baines et al. 2010; Boyajian et al. 2012, 2013; Maestro et al. 2013; von Braun et al. 2014; Boyajian et al. 2015; Kane et al. 2015; Ligi et al. 2016; White et al. 2018; Karovicova et al. 2020, 2022a, 2022b). This sample was further pruned for validation, by requiring that there be at least four optical photometric measurements ($\lambda < 1 \mu\text{m}$) retained after outlier-photometry clipping for the SED fitting. Since CHARA stars are preferentially bright, this criterion essentially requires the availability of Gaia G , Hipparcos H_p , and Tycho2 B_T and V_T photometry. We then performed the SED fitting using interferometric T_{eff} and spectroscopic $\log g$ values as priors (taken from the aforementioned references).

The angular diameter comparison shown in Figure 3 yields good agreement, with an offset of 3.07% (SED/CHARA) and a scatter of 6.77%. Inspecting the stars with angular diameters in the range $1 < \theta/\text{mas} < 3$, particularly for dwarfs/subgiants (blue squares in the top panel), suggests that our angular diameters could be overestimated. This overestimation is

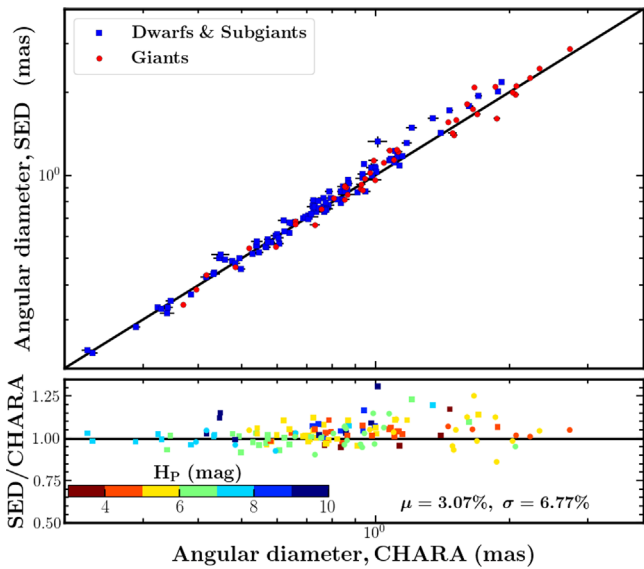


Figure 3. Comparison of angular diameters from the SED fitting with those from CHARA interferometry. Top: angular diameters compared for the 83 dwarfs and subgiants ($\log g > 3.5$; blue squares) and the 33 giants ($\log g \leq 3.5$; red circles). The one-to-one line (perfect match) is shown in black. Bottom: angular diameter ratio (SED/CHARA) shown for the same set of populations, but color-coded by Hipparcos H_p magnitude. The mean and the standard deviation of the ratios are also labeled.

probably caused by saturated photometry, since the dwarfs/subgiants in this angular diameter range are very bright. We note that this offset is smaller than that found by Tayar et al. (2022), who compared interferometric angular diameters from CHARA with different beam combiners, yielding a systematic median difference of 4%.

3.2. HST Spectrophotometry

The best way to validate bolometric flux so far probably has been using HST/STIS CALSPEC spectrophotometry. There is evidence to suggest that its *relative* fluxes from the visible to the near-IR wavelength of $2.5 \mu\text{m}$ are currently precise to $\sim 1\%$ for the primary reference standards (Bohlin et al. 2014). Meanwhile, the bolometric corrections serve as an alternative approach to estimate the bolometric flux (Casagrande & Vandenberg 2018). We use the same sample of the HST/STIS CALSPEC primary flux standards as Casagrande & Vandenberg (2018) for our validation.

Figure 4 compares our bolometric flux with that calculated from the CALSPEC spectrophotometry, revealing a scatter of 1.99%. This small scatter demonstrates that our SED fitting is precise, given that the CALSPEC spectrophotometry is precise to $\sim 1\%$. We notice a somewhat large offset of 3.41%, in the sense that our bolometric flux is larger. The reason for this offset is uncertain, given that the CALSPEC spectrophotometry was largely well calibrated to reach high precision. We note that although Casagrande & Vandenberg (2018) attained a sub-1% offset between their bolometric flux scale derived from bolometric corrections and those from CALSPEC spectrophotometry, their scale was based on their adopted value of solar absolute magnitude. As pointed out by Casagrande & Vandenberg (2018), solar absolute magnitude is an arbitrary zero-point, and any value is equally legitimate on the condition that once chosen all bolometric corrections are scaled accordingly. On the other hand, an independent comparison

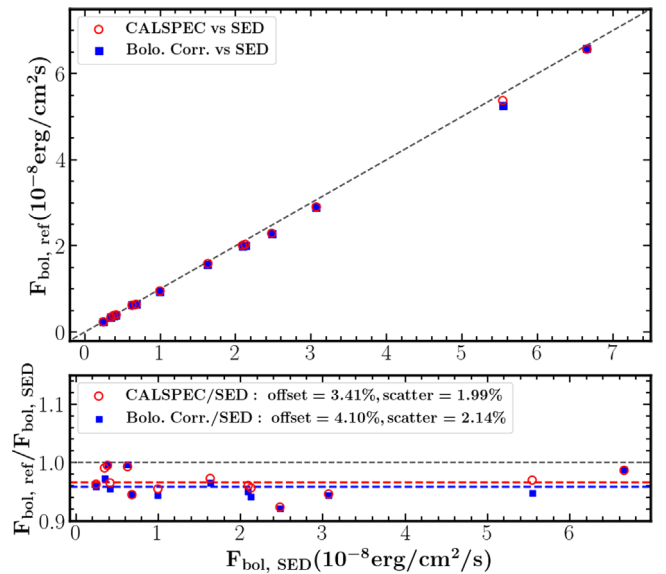


Figure 4. Top panel: comparison of bolometric flux derived from the SED fitting with that computed from the HST CALSPEC/STIS spectrophotometry of flux standards (red circles; Bohlin et al. 2014) and with that calculated from bolometric corrections (blue squares; Casagrande & Vandenberg 2018). The dashed line marks the one-to-one relation. Bottom panel: bolometric flux ratio as a function of our bolometric flux estimates. The red and blue dashed lines show the mean ratios, while the gray dashed line denotes perfect one-to-one agreement. The numbers in the legend indicate the offsets and the scatters.

of luminosities between the SED fitting and asteroseismology reveals a sub-1% offset (see next section). This suggests that our bolometric flux scale is not necessarily the root cause of the 3.41% offset, and the bias of the absolute scale of CALSPEC spectrophotometry, if any exists, could contribute to this offset.

3.3. Asteroseismology

In this section, we validate our estimates of radius, luminosity, and extinction with asteroseismic counterparts from the APOKASC catalogs for dwarfs and subgiants (Serenelli et al. 2017) and for giants (Pinsonneault et al. 2018). These two studies leveraged asteroseismic constraints with SDSS *griz* photometry and APOGEE spectroscopy to determine stellar parameters, using a grid-based modeling method for dwarfs and subgiants (Serenelli et al. 2017) and an empirical method for giants (Pinsonneault et al. 2018). Their robust zero-point calibration of stellar parameters enables us to test the accuracy and precision of our results. We also compare our parameter estimates with the latest, homogeneous Kepler stellar properties catalog (Berger et al. 2020), which was based on a grid-based modeling approach, independent of asteroseismology. It is important to note that for our SED fitting we used the same T_{eff} , $\log g$, and metallicity values as Serenelli et al. (2017), Pinsonneault et al. (2018), and Berger et al. (2020) did, rather than the latest catalog we compiled in Section 2.1, to eliminate the systematics caused by different atmospheric parameter scales.

3.3.1. Radii

Figure 5 shows good consistency between radii derived from our SED fitting and those from asteroseismology, with an offset of 0.1% and a scatter of 4.9%. The comparison between our radius estimates and those from the Kepler stellar property catalog (Berger et al. 2020) also yields good agreement, with

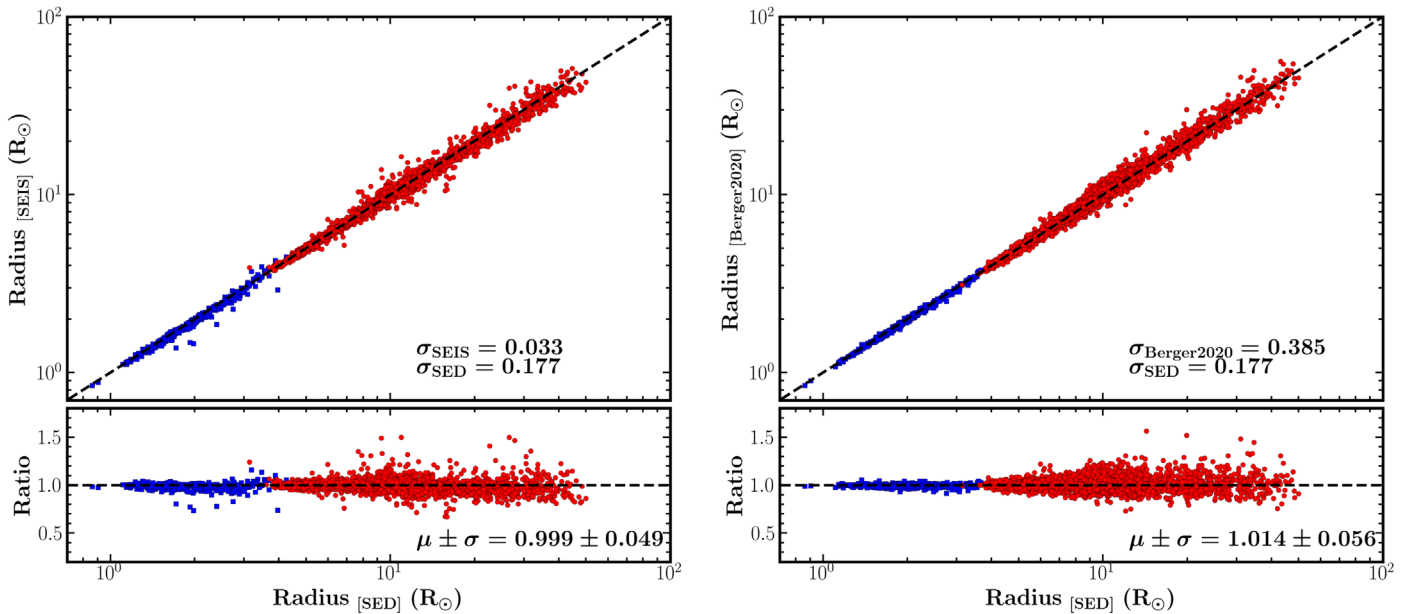


Figure 5. Left: comparison of radii determined from the SED fitting with those from asteroseismology. The blue squares indicate dwarfs and subgiants from Serenelli et al. (2017), while the red circles indicate giants from Pinsonneault et al. (2018). The median formal uncertainties of the two sets of radii are shown in the top panel, and the mean ratio of the seismic to SED fitting radii and its standard deviation are given in the bottom panel. The dashed lines represent perfect consistency. Right: similar to the left panels, except for the seismic radii replaced by those from Berger et al. (2020).

an offset of 1.4% and a scatter of 5.6%. In both comparisons, we find a smaller dispersion in dwarfs (blue circles) than in giants (red circles). This is in line with the fact that the giants are more distant compared to the dwarfs and are thus subject to larger uncertainties in parallax and distance.

Our independent radius estimates provide an opportunity to test how well the seismic scaling relations have been empirically calibrated by Pinsonneault et al. (2018). We note that the asteroseismic radius scale of red giants by Pinsonneault et al. (2018) was calibrated to match the fundamental measurement of the mean mass of red giant branch (RGB) eclipsing binary stars in two open clusters. As Pinsonneault et al. (2018) pointed out, their asteroseismic radius scale for core helium burning (CHeB) stars should be used with caution because the uncertain mass loss on the RGB complicates an absolute radius calibration for CHeB stars. Thus, their CHeB radius scale was assumed to be the same as that for RGB stars. Since our radius scale is not affected by population type (RGB or CHeB), the strong one-to-one correlation between the radii from Pinsonneault et al. (2018) and our measurements would suggest a high degree of self-consistency in their asteroseismic radius scale.

Asteroseismology has been extensively used to test the zero-points of Gaia parallaxes released in Gaia DR1, DR2, and EDR3, by comparing radius and/or parallax (e.g., Davies et al. 2017; Huber et al. 2017; Hall et al. 2019; Khan et al. 2019; Zinn et al. 2019; Zinn 2021). We stress that our radius scale matches the asteroseismic radius scale at a level of sub-1%, confirming asteroseismic findings of the reduced parallax systematics in Gaia EDR3 (e.g., Zinn 2021) compared to those from the previous data releases.

3.3.2. Luminosities

In Figure 6, we compare the luminosities inferred from the SED fitting with those from asteroseismology (Serenelli et al. 2017; Pinsonneault et al. 2018) and from the Kepler stellar

properties catalog by Berger et al. (2020). Our luminosity estimates are consistent with the asteroseismic values, with a mean offset of -0.004 and a dispersion of 0.042 . Meanwhile, our estimates are also in good agreement with those from Berger et al. (2020), with a mean offset of 0.008 and a dispersion of 0.053 . We note that our luminosity scale is well in line with the literature studies.

3.3.3. Extinction

Figure 7 shows a comparison between the extinctions obtained from our SED fitting and those from the APOKASC2 catalog by Pinsonneault et al. (2018). The comparison yields a mean offset of -0.039 and a standard deviation of 0.050 . The bottom panel of Figure 7 shows that the extinction residuals tend to get smaller with increasing extinction. We remind that their seismic extinctions were derived by comparing apparent magnitudes with absolute magnitudes, which were calculated from seismic luminosities and bolometric corrections. Since our luminosities are consistent with those from APOKASC2, any uncertainty in the zero-points of the seismic scaling relations, if at all, should not contribute to this systematic extinction offset. The different extinction laws used in both studies should not lead to this offset either, as discussed in Section 2.5.

It is quite likely, therefore, that the main reason behind this discrepancy is related to the bolometric correction scale adopted by Pinsonneault et al. (2018). We remind the reader that to estimate stellar parameters (e.g., luminosity) from apparent magnitudes and Gaia parallaxes, both the direct method (more specifically, bolometric corrections) and the SED fitting method depend on the choice of spectral libraries and photometric systematic parameters (e.g., zero-points of the flux densities and filter transmission curves). Any difference in these input data can lead to this small but statistically significant A_V offset. We note that Pinsonneault et al. (2018) used ATLAS9, whereas we used MARCS for this sample of

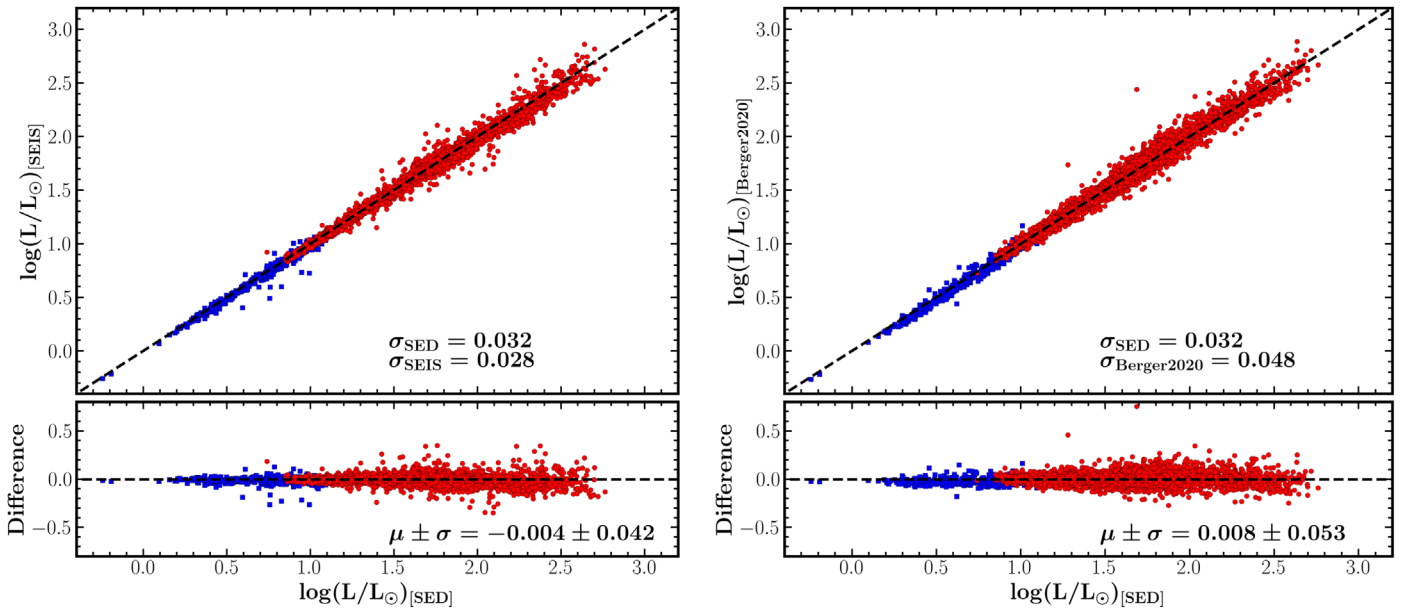


Figure 6. Left: comparison of luminosity determined from the SED fitting with those from asteroseismology. The symbols, line, and text have the same meaning as in Figure 5, now for luminosity. Right: similar to the left panels, except for the seismic luminosity replaced by those from Berger et al. (2020). Our SED luminosities are computed from our bolometric fluxes and Gaia-based distances (Bailer-Jones et al. 2021), while the luminosities from asteroseismology and Berger et al. (2020) were derived from their radii and temperatures.

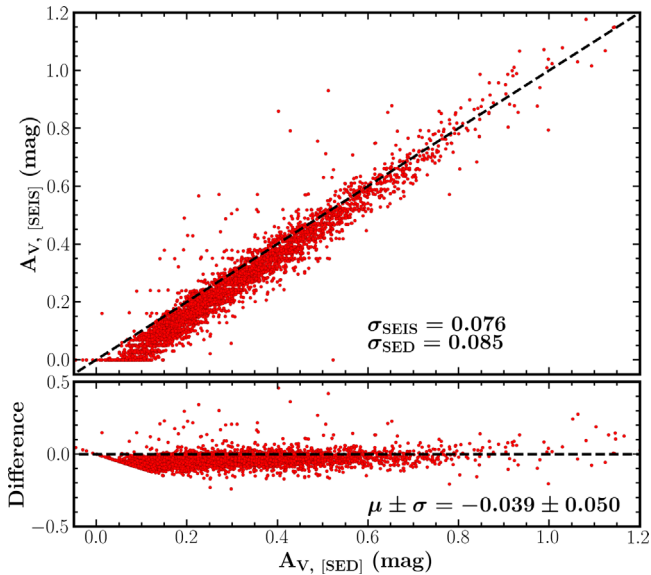


Figure 7. Comparison of extinctions determined from the SED fitting with those from asteroseismology. The symbols, line, and text have the same meaning as in Figure 5. No extinctions were provided for dwarfs and subgiants by Serenelli et al. (2017).

red giants. Furthermore, a bolometric correction is tied to a chosen reference value for absolute solar magnitude, which should be appreciated as a definition, rather than a measurement (Casagrande & Vandenberg 2014), and can thus be subject to systematic difference in the literature. For example, Girardi et al. (2002) used $M_{\text{bol},\odot} = 4.77$ mag, Casagrande & Vandenberg (2014) used $M_{\text{bol},\odot} = 4.75$ mag, and the IAU 2015 Resolution B2 recommended $M_{\text{bol},\odot} = 4.74$ mag. These values translate to differences in bolometric flux of up to 1.2%.

We also compared our extinction scale with that from Berger et al. (2020), yielding an offset of 0.02 with a scatter of 0.108 (figure not shown here). This A_V offset is smaller than the offset

found with respect to Pinsonneault et al. (2018). We also note that the extinction difference between our SED fitting and Berger et al. (2020) is a stable function of extinction. We recall that the Berger et al. (2020) extinction estimates were taken from the 3D Bayestar dust map (Green et al. 2019). Indeed, our extinction scale is well consistent with that of Green et al. (2019) (see Section 4.2), in line with the comparison result presented here.

4. Results

We now present our radius and extinction estimates for 1.5 million APOGEE, GALAH, and RAVE stars.

4.1. T_{eff} -Radius Diagram

Figure 8 shows our radius estimates in a T_{eff} -radius diagram, color-coded by the normalized number density. Several evolutionary features stand out. In giants, we observe the red clump and its extension toward the horizontal branch up to $T_{\text{eff}} \simeq 6000$ K. Below the lower envelope of the red clump is the presence of the RGB bump. We recall that the RGB bump is the result of an accumulation of stars, due to a temporal decrease and subsequent increase of luminosity along the RGB. This phenomenon is linked to the approach of the hydrogen-burning shell to the composition discontinuity left behind by the first dredge-up (Hekker et al. 2020, and references therein).

A morphologically similar evolutionary phase is the asymptotic giant branch (AGB) bump. At the beginning of the AGB phase, the He-exhausted core contracts and heats up, and the H-rich envelope expands and cools so effectively that the H-burning shell that lies above the He-burning shell extinguishes. The expansion of the envelope is eventually halted by its own cooling, and it recontracts. The luminosity then decreases, and the matter at the base of the convective envelope heats up. When the H-burning shell reignites, the luminosity increases again. The decrease and subsequent increase of the luminosity produce a bump along the AGB

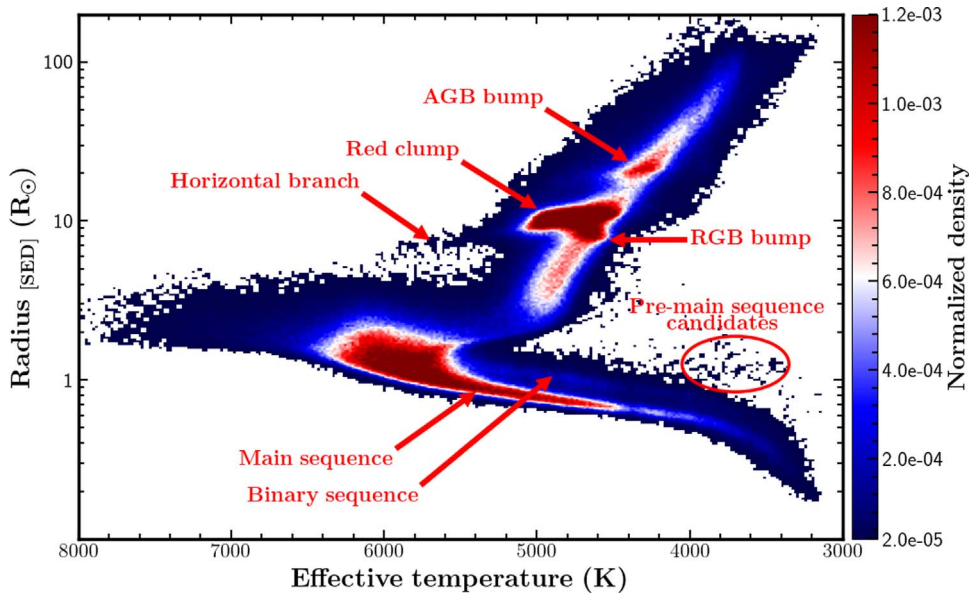


Figure 8. Radius vs. T_{eff} diagram, color-coded by the normalized number density. Radius estimates are derived from our SED fitting, while effective temperatures are adopted from APOGEE DR17, GALAH DR3, and RAVE DR6. Some key features are highlighted.

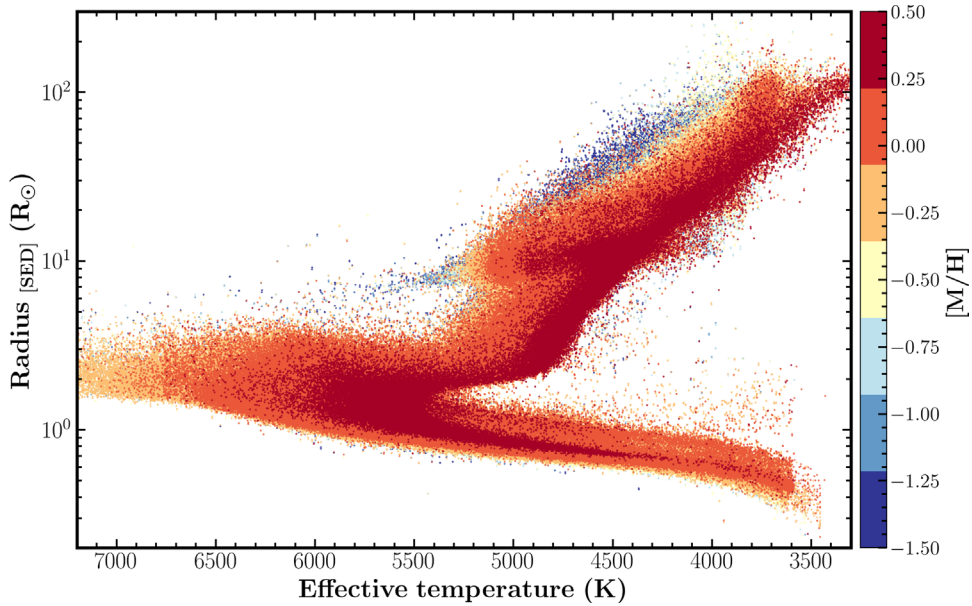


Figure 9. Similar to Figure 8, except for the color code replaced by spectroscopic metallicities from APOGEE DR17, GALAH DR3, and RAVE DR6, available for stars with $T_{\text{eff}} \gtrsim 3500$ K.

(Ferraro 1992; Gallart 1998). A clear low-density gap between the red clump and the AGB bump is seen in Figure 8. Dréau et al. (2021) found that at the very early phase of the AGB evolution the star evolves faster before reaching the AGB bump, leading to a lower chance of observing stars in this gap.

Another prominent feature is the binary sequence, which runs slightly above and almost parallel to the MS. It is composed of photometrically unresolved binaries. In addition, a number of APOGEE stars are present above the MS and the binary sequence. We find that these stars also stand out in the APOGEE $T_{\text{eff}}\text{-}\log g$ diagram, and are linked to rotational variables, as recognized by Jayasinghe et al. (2021) with ASAS-SN light curves (see their Figure 7). We find that these stars exhibit high infrared excess (traced with 2MASS K_s and

ALLWISE W3 magnitudes; Yu et al. 2021) and hence are pre-MS star candidates.

Our radius estimates reveal expected metallicity effects on stellar evolution, shown in Figure 9. We observe a metallicity gradient, particularly in red giants, where metal-poor stars have higher temperatures at a given radius than metal-rich stars do. Meanwhile, the red clump and its extension toward the horizontal branch are also visible, as is the metallicity gradient in this population.

Our SED fitting method, in combination with Gaia parallaxes, is efficient for detecting double-lined (SB2) spectroscopic binary candidates. Figure 10 shows a clear binary sequence (orange circles) located above the MS (black circles). To separate this binary sequence, first, we identified MS stars by binning T_{eff} and

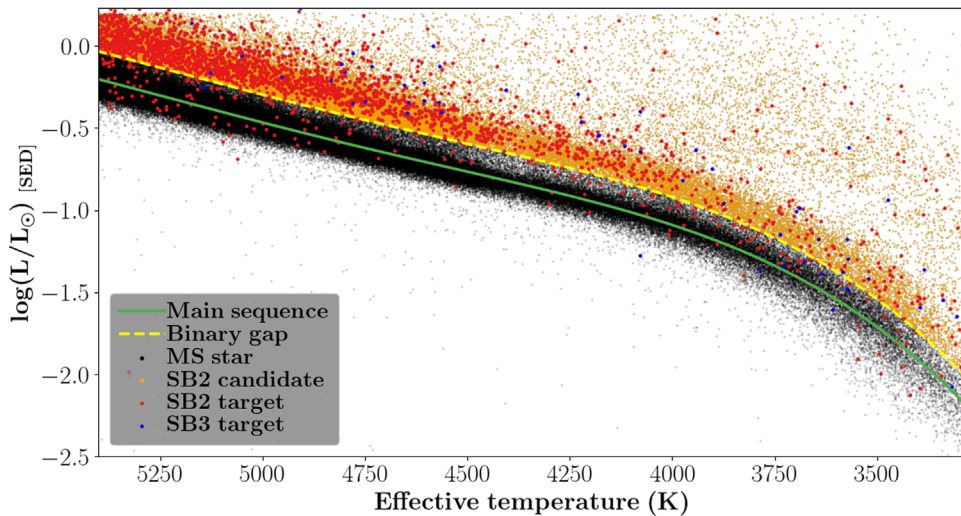


Figure 10. Hertzsprung–Russell (H-R) diagram. The black circles mark MS stars, and the orange circles denote our SB2 candidates. The red and blue circles are SB2 and SB3 candidates/binaries compiled from the literature, respectively. The yellow dashed line indicates the gap between the SB2 sequence and the MS (green line; see the text).

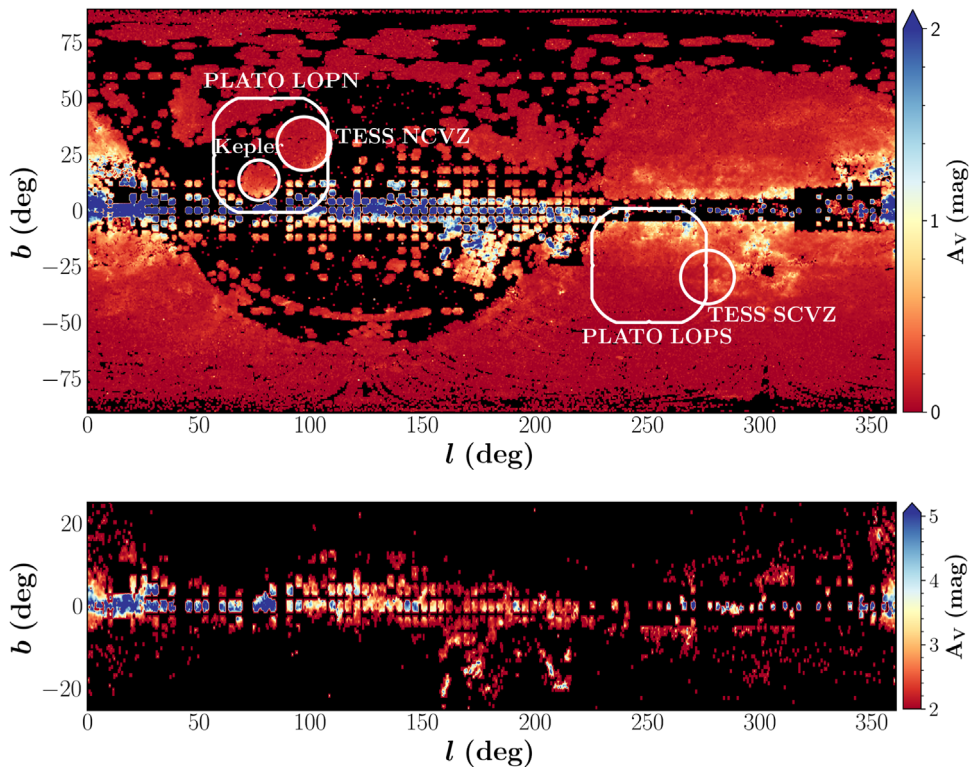


Figure 11. Top: extinction map in Galactic coordinates, traced by the footprint of APOGEE DR17, GALAH DR3, and RAVE DR6. The Kepler field, TESS Northern and Southern Continuous Viewing Zones (NCVZ, SCVZ), and PLATO North and South Long-duration Observation Phase fields (LOPN, LOPS) are schematically highlighted. The sky region that has not been observed by the three spectroscopic surveys is shown in black. Bottom: similar to the top panel, except for highlighting the Galactic plane using the stars with $A_V > 2$ mag (note the different A_V scales of the color bars).

locating the MS star group from the bimodal distribution of luminosity in each T_{eff} bin of 100 K. Then, we fitted a fourth-order polynomial to all these MS stars, shown with the green solid line.¹⁴ Next, with this polynomial, we predicted luminosities given T_{eff} and subtracted these from the measured luminosities. The luminosity residuals show a bimodal distribution, where the valley is at $\delta \log(L/L_{\odot}) = 0.17$ dex. Finally, we defined the

¹⁴ The optimized polynomial coefficients from high to low orders are $-1.186\text{E-}13$, $2.341\text{E-}9$, $-1.725\text{E-}5$, $5.691\text{E-}2$, and $-7.216\text{E}1$.

stars shown in Figure 10 as SB2 candidates if their luminosities are higher than their predicted luminosities by > 0.17 dex.

This binary sequence well overlaps with the SB2 stars/binaries candidates previously found with APOGEE, GALAH, RAVE, and Gaia RVS spectra (Matijevic et al. 2010; Traven et al. 2020; Kounkel et al. 2021; Gaia Collaboration et al. 2022). We reported a detection of 43,054 SB2 candidates/binaries, among which 36,854 are new SB2 candidates and can be selected from Table 4 by requiring `BinarySource=SED`. We recommend spectroscopic follow-up observations of these candidates to

confirm the classifications and to characterize their orbital properties.

4.2. All-sky Dust Map

Figure 11 shows our extinction map, traced by the footprint of the three spectroscopic surveys, covering low- (RAVE), intermediate- (GALAH), and high-extinction (APOGEE) sky regions. As expected, we observe high extinctions along the Galactic plane and lower extinctions toward higher latitudes. Differential extinction is visible in the regions dedicated for asteroseismic analyses and exoplanet studies, e.g., the Kepler field (Borucki et al. 2010), TESS Northern and Southern Continuous Viewing Zones (NCVZ, SCVZ; Ricker et al. 2015), and PLATO North and South Long-duration Observation Phase fields (LOPN, LOPS; Nascimbeni et al. 2022).

Next, we analyzed the accuracy and precision of our extinction estimates by comparing them with the large-volume extinction studies of the *StarHorse* catalog (Queiroz et al. 2020) and the 3D *Bayestar* dust map (Green et al. 2019). The *StarHorse* extinctions were obtained through a grid-based modeling approach by combining spectroscopic data from APOGEE DR16, GALAH DR2, and RAVE DR6 surveys; parallaxes from Gaia DR2; and photometry from Pan-STARRS, 2MASS, and AllWISE (Queiroz et al. 2020). The *Bayestar* reddenings were acquired through a Bayesian, model-independent scheme by integrating Gaia parallaxes from Gaia DR2 and photometry from Pan-STARRS and 2MASS (Green et al. 2019). Note that we used $R(V) = 3.1$, when converting *Bayestar* $E(B-V)$ to A_V via $A_V = R(V)E(B-V)$, for consistency (see Section 2.5). This is equivalent to comparing our $E(B-V)$ estimates with those from Green et al. (2019).

In Figure 12(a), we compare our A_V estimates that are independent of stellar evolutionary models with those from Queiroz et al. (2020), yielding a tight correlation with a scatter of 0.24. However, a significant scale difference is visible, with a slope of 1.20 and an intercept of -0.10 . It is important to recall that Queiroz et al. (2020) used different data releases of spectroscopic data sets (APOGEE DR16, GALAH DR2, RAVE DR6) than ours (APOGEE DR17, GALAH DR3, RAVE DR6). We then repeated our fitting analysis with their input spectroscopic data and found that the significant A_V scale difference remains. Specifically, the A_V difference caused by the different spectroscopic data releases is 0.01 ± 0.13 mag, without any systematic trend. Since our SED fitting analysis is more sensitive to T_{eff} than $\log g$ and metallicity, we conclude that the different T_{eff} scale, which is 18 ± 93 K, cannot lead to the significantly different A_V scale shown in Figure 12(a).

In Figure 12(b), we then compare our A_V estimates with those from Green et al. (2019), yielding a larger dispersion of 0.30 but with a good scale consistency (slope = 1.00, intercept = 0.09). This dispersion is smaller when comparing the extinctions from Queiroz et al. (2020) and Green et al. (2019) ($\sigma = 0.35$), as shown in Figure 12(c). This suggests that our extinction estimates are more precise than those from Queiroz et al. (2020). Our choice of using 32 bandpasses, which is more than the number used in Queiroz et al. (2020), is likely to be responsible for this.

In Figure 12(a), we observe a number of stars with low extinctions from our work and high values determined by Queiroz et al. (2020), namely the stars located above the red line ($A_V \lesssim 0.5$ mag; lower left corner). These stars are present

below the red line in the lower left corner of Figure 12(c). Given that these stars are not outliers in Figure 12(b), this would suggest that for these stars the extinctions of Queiroz et al. (2020) are overestimated.

In addition to the feature in the low-extinction regime, a larger scatter is visible in the high-extinction range, as shown in Figures 12(b) and 12(c). Now, we focus on the sample of stars with high extinctions of $A_V > 5$ mag to understand the precision of each extinction scale. These stars are shown in dereddened color-magnitude diagrams in Figure 13. First, we see that the AGB population is the most scattered if the extinctions of Green et al. (2019) are used (Figure 13(a)); the population is less scattered when our extinctions are used (Figure 13(b)), and it is the least scattered when the extinctions of Queiroz et al. (2020) are used (Figure 13(c)). The same conclusion applies to the scatter (elongation) of the red clump. The different A_V precisions rely on the amount of observational data used (photometry, spectroscopy, and/or astrometry), as well as on the extent of stellar models involved (see the legend of Figure 13). Overplotted are the MIST evolutionary models of the AGB phase with various reasonable masses ($M = 0.8, 1.0, 1.2 M_{\odot}$) and metallicities ($[M/H] = 0.3, 0, -0.3$) (Choi et al. 2016; Dotter 2016). We can see that the models better match the observations if our extinctions, or those from Green et al. (2019), are used.

In summary, our extinction scale is consistent with Green et al. (2019) at the $<1\%$ level and deviates from Queiroz et al. (2020) by $\sim 20\%$. Our extinction scale and that of Green et al. (2019) better match the MIST evolutionary models than Queiroz et al. (2020). Globally, our extinctions have the highest precision (see the scatter values annotated in Figure 12), probably due to the use of a higher number of photometric bandpasses. The extinction values from our work and Green et al. (2019) are more consistent in low-extinction regimes ($A_V \lesssim 0.5$ mag). Based on the analysis above, we keep our extinction scale as it is, i.e., without a calibration onto a reference scale.

4.3. Extinctions of Gaia Open Clusters

After fixing our extinction scale, we then used the extinctions of individual stars to determine the global extinctions of 184 Gaia open clusters, with the membership classifications from Cantat-Gaudin et al. (2020). Each of these clusters has at least three members in our sample. We adopted the median extinction of the stars in each cluster to estimate the global cluster extinction. We approximated its uncertainty by summing up in quadrature the median formal uncertainty and a statistical uncertainty σ/\sqrt{N} , where σ is the standard deviation of the extinction estimates of cluster members and N is the number of stars in the cluster. Table 3 lists the extinctions and their uncertainties for these 184 Gaia open clusters.

Figure 14 shows a comparison of the extinctions for 184 open clusters derived from our work with those from Cantat-Gaudin et al. (2020). Cantat-Gaudin et al. (2020) estimated their average cluster extinctions by training an artificial neural network with Gaia photometry (i.e., color-magnitude diagrams) and Gaia parallaxes. We observe a good consistency in Figure 14, with a mean difference of -0.09 mag and a standard deviation of 0.34 mag, in the sense that the Cantat-Gaudin et al. (2020) extinction scale is on average slightly lower than ours.

Figure 14 also shows that in the high-extinction regime ($A_V \gtrsim 2.5$ mag) the A_V estimates from Cantat-Gaudin et al. (2020)

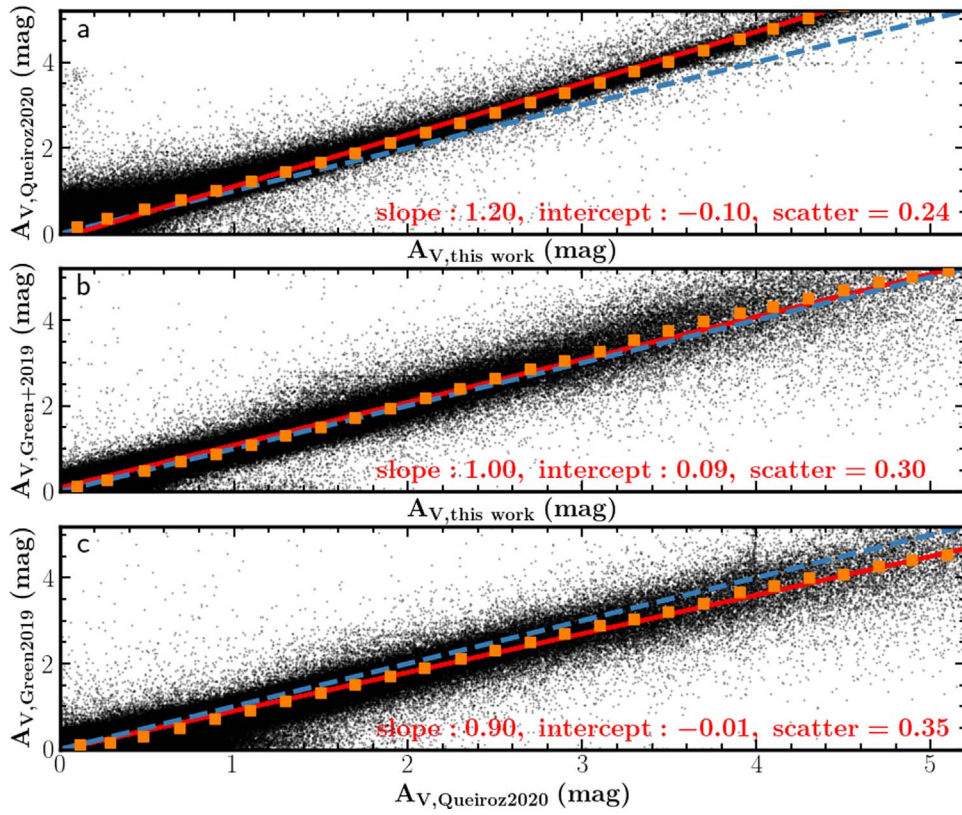


Figure 12. Comparisons between extinctions derived from the SED fitting and those from Queiroz et al. (2020) and Green et al. (2019). In each panel, the orange diamonds show the mean values in each bin, and the red line is a fitted linear model to the orange diamonds, with its slope and intercept values annotated. The scatter value is the dispersion of the A_V measurements with respect to the fitted linear model. The blue dashed line indicates the one-to-one correspondence.

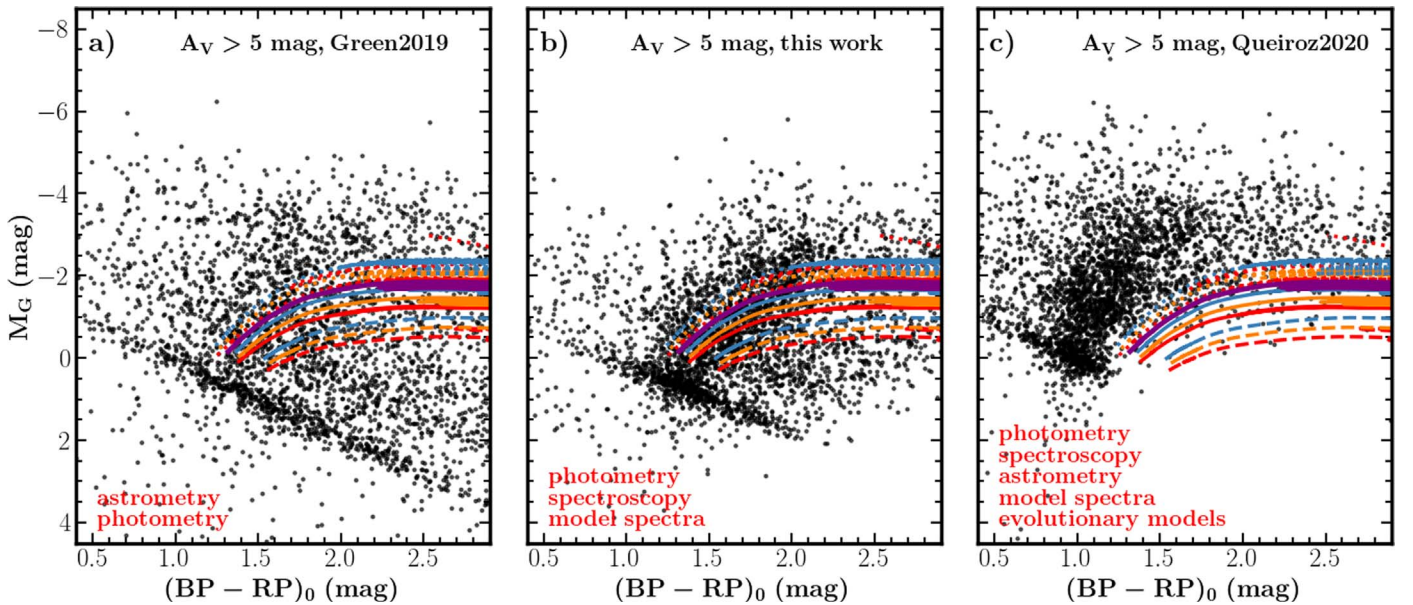


Figure 13. Dereddened Gaia color–magnitude diagram of high-extinction, high-luminosity red giants ($A_V > 5$ mag), using A_V from (a) Green et al. (2019), (b) this work, and (c) Queiroz et al. (2020). The red text indicates the data and models used for deriving A_V in each work. Overplotted are MIST evolutionary tracks of the AGB phase of different reasonable masses and metallicities: dashed, solid, and dotted lines for $[M/H] = 0.3, 0,$ and -0.3 , respectively, and red, orange, and blue lines for $M = 0.8, 1.0,$ and $1.2 M_\odot$, respectively. The purple line corresponds to a stellar track of $M = 1.0 M_\odot$ and $[M/H] = 0$ that has representative properties of the sample shown here.

are globally smaller than ours. This is consistent with their findings when comparing their predicted A_V estimates with those from their training sample and with the independent literature study in Kharchenko et al. (2013, see their Figure 5). The reason

for this A_V underestimation is that there are few open clusters with $A_V \gtrsim 2.5$ mag in their training set. It is well known that statistical inference on small samples leads to inferior estimates in training and consequently to reduced performances in prediction.

Table 3
Global Extinctions of 184 Gaia Open Clusters

Cluster	l (deg)	b (deg)	$A_{V,NN}$ (mag)	A_V (mag)	σ_{A_V} (mag)	N
NGC 6819	73.982	8.481	0.40	0.53	0.16	49
NGC 1817	186.193	-13.032	0.59	0.64	0.15	49
Blanco 1	15.090	-79.086	0.01	-0.01	0.13	51
NGC 2204	226.016	-16.114	0.01	0.27	0.17	59
NGC 188	122.837	22.373	0.21	0.29	0.17	60
NGC 2244	206.361	-2.026	1.46	1.34	0.19	60
NGC 2158	186.635	1.788	1.44	1.46	0.18	67
Ruprecht 147	20.930	-12.760	0.06	0.30	0.16	68
NGC 6791	69.964	10.906	0.70	0.41	0.19	77
Melotte 20	147.357	-6.404	0.30	0.23	0.15	81
NGC 7789	115.527	-5.366	0.83	0.87	0.15	88
NGC 752	136.959	-23.289	0.07	0.12	0.16	110
Melotte 25	179.767	-21.164	0.00	0.11	0.15	118
Collinder 261	301.696	-5.537	0.81	0.90	0.14	216
NGC 2168	186.609	2.230	0.46	0.61	0.15	225
NGC 2632	205.952	32.428	0.00	0.11	0.15	228
Melotte 22	166.462	-23.614	0.18	0.17	0.15	269
NGC 2682	215.691	31.921	0.07	0.11	0.16	350

Note. The second and third columns are the Galactic latitude and longitude of the center of each cluster, respectively, and the fourth column is the extinction estimate, all taken from Cantat-Gaudin et al. (2020). The fifth, sixth, and seventh columns are the extinction estimate, its uncertainty, and the number of members, all from this work. See the text for the definition of the extinction uncertainty. Only those clusters that have at least 49 members observed by APOGEE, GALAH, or RAVE are shown here. The entire table for 184 Gaia open clusters with at least three members each is available online.

(This table is available in its entirety in machine-readable form.)

Next, we discuss two open clusters, NGC 6791 and NGC 6819, that have gained tremendous importance and have been subject to extensive asteroseismic analyses owing to the availability of exquisite Kepler data. For NGC 6791, our analysis yields $E(B-V) = 0.13 \pm 0.06$ mag (or $A_V = 0.41 \pm 0.19$ mag, adopting $R(V) = 3.1$), consistent with the literature value of $E(B-V) = 0.10-0.16$ (An et al. 2015 and references therein) and close to $E(B-V) = 0.16 \pm 0.025$ mag, as obtained from asteroseismic analysis by Wu et al. (2014) and Brogaard et al. (2021). We note that Brogaard et al. (2021) also reported a second value, $E(B-V) = 0.13$ mag supported by their analysis, in line with ours. For NGC 6819, we obtained a reddening value of $E(B-V) = 0.17 \pm 0.05$ mag (or $A_V = 0.53 \pm 0.16$ mag). This is consistent with the asteroseismic value evaluated by Handberg et al. (2017), $E(B-V) = 0.15$ mag, as well as the results in Bragaglia et al. (2001; $E(B-V) = 0.142 \pm 0.044$ mag) and Rosvick & Vandenberg (1998; $E(B-V) = 0.16$ mag).

Our extinction estimates of the members of NGC 6791 and NGC 6819 allow insights into their potential differential reddening, a feature that is usually identified by the spread of the upper MS in color-magnitude diagrams. Indeed, Brogaard et al. (2012) found evidence in favor of differential reddening in NGC 6791 but warned that systematic effects from instrument photometry and/or the reduction procedure may also be present in their findings. We note that their reported differential reddening is $\Delta E(B-V) = \pm 0.04$ mag, which is at the same level as their color precision. As shown in Figure 15, our extinction estimates reproduce the major differential extinction features seen in Brogaard et al. (2012). For example,

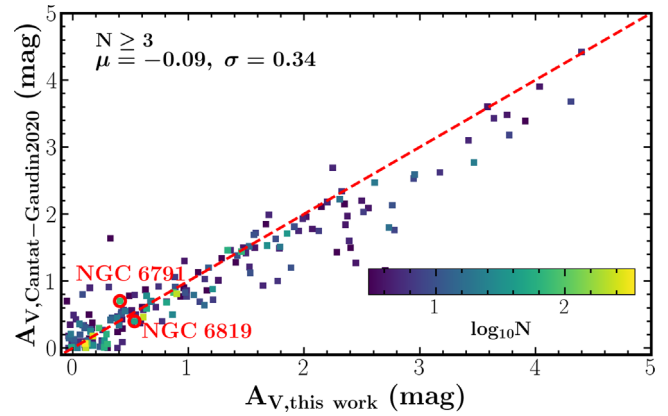


Figure 14. Comparison of extinctions of 184 Gaia open clusters that have been investigated by Cantat-Gaudin et al. (2020) and that have at least three members each in our sample. The color code indicates the number of members of each cluster. Two open clusters, NGC 6791 and NGC 6819, that are subject to extensive asteroseismic analysis are highlighted with red open circles. The red dashed line shows the one-to-one relation. The mean difference (-0.09) and its standard deviation (0.34) are indicated, where the literature extinction scale is on average less than ours.

for NGC 6791, we also find low extinction around $(X, Y) = (200, 100)$. Meanwhile, Platais et al. (2013) found a maximum differential reddening of $\Delta E(B-V) = 0.06$ mag in NGC 6819. A key feature revealed therein is the presence of a local high-extinction region, expected in the direction from the cluster center toward the lower right corner of the right panel of Figure 15. Indeed, our results support the finding by Platais et al. (2013). While our analysis of differential reddening is limited by the spatial resolution owing to a relatively small sample size, the high precision of extinction measurements enables us to confirm the existence of the differential extinction in both NGC 6791 ($A_V = 0.18-0.63$ mag) and NGC 6819 ($A_V = 0.42-0.63$ mag).

5. Catalog

We present our final catalog in Table 4. It offers homogenized atmospheric parameter estimates and their uncertainties for stars in APOGEE DR17, GALAH DR3, and RAVE DR6. It also provides derived parameter values from our SED fitting analysis, namely radii, luminosities, extinctions, bolometric fluxes, and angular radii, together with other data sets for user convenience.

Figure 16 shows the resultant uncertainty distributions of our derived parameters. Our catalog median precision is 6.9% for angular radius, 8.2% for bolometric flux, 0.14 mag for extinction, 7.4% for radius, and 9.4% for luminosity (0.04 dex for $\log(L/L_\odot)$). Note that we added in quadrature a 2.4% uncertainty floor to the random T_{eff} uncertainties (Tayar et al. 2022), which affects all of the conservative uncertainty distributions shown in Figure 16. The distribution of extinction uncertainty is bimodal. This is because the majority of the APOGEE stars (95.5%), which are globally distant, are included in the right peak, while GALAH and RAVE stars, which are typically nearby, are nearly equally distributed in both peaks.

Our catalog is subject to two caveats. First, the derived parameters for photometrically unresolved binaries could be biased by the combined photometry of binary components. For this, we added in Table 4 the column `BinarySource`, to select/reject confirmed or candidate binary systems. This lists

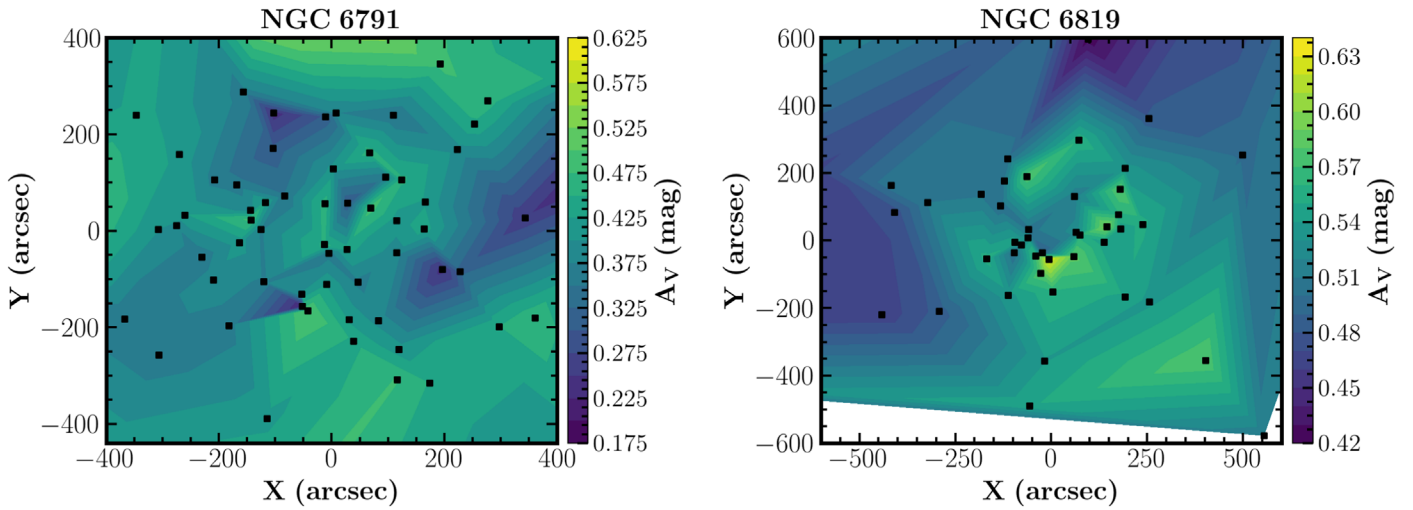


Figure 15. Spatial distributions of the extinctions of NGC 6791 with respect to the cluster center (R.A., decl.) = (295.32283, 40.19639) and of NGC 6819 with respect to the cluster center (R.A., decl.) = (295.32283, 40.19639). The black circles indicate the cluster star members (Cantat-Gaudin et al. 2020) in our sample that are used to probe differential extinction as shown with the filled contours. The margin at the bottom of the right panel is not covered by any stars. For comparison, our field windows shown here are chosen to be the same as in Brogaard et al. (2012) for NGC 6791 and in Platais et al. (2013) for NGC 6819.

Table 4
SED-fitting-based Stellar Parameters of ~ 1.5 Million Stars

Label	Units	Description
starID		APOGEE_ID for APOGEE, subject_id for GALAH, and raveid for RAVE
Gaia		Gaia DR3 or EDR3 source_id
Teff	K	calibrated T_{eff}
e_Teff	K	rescaled T_{eff} uncertainties, including a 2.4% error floor determined with interferometry.
logg	dex	calibrated $\log g$
e_logg	dex	rescaled $\log g$ uncertainties
FeH	dex	calibrated [Fe/H]
e_FeH	dex	rescaled [Fe/H] uncertainties
Dist	pc	Bailer-Jones et al. (2021) distances, $r_{\text{med_photgeo}}$ preferred if available, otherwise $r_{\text{med_geo}}$
e_Dist	pc	Bailer-Jones et al. (2021) distance uncertainties, $(r_{\text{hi_photgeo}} - r_{\text{lo_photgeo}})/2$ preferred if available, otherwise $(r_{\text{hi_geo}} - r_{\text{lo_geo}})/2$
Av	mag	extinction in V , assuming $R(V) = 3.1$
e_Av	mag	extinction uncertainty in V
Fbol	$\text{erg s}^{-1} \text{cm}^{-2}$	bolometric flux
e_Fbol	$\text{erg s}^{-1} \text{cm}^{-2}$	bolometric flux uncertainty
angRad	mas	angular radius
e_angRad	mas	angular radius uncertainty
logL	dex	luminosity, $\log(L/L_{\odot})$
e_logL	dex	luminosity uncertainty
radius	R_{\odot}	radius
e_radius	R_{\odot}	radius uncertainty
npoint		number of photometric points used for the SED fitting
source		target source, i.e., APOGEE DR17, GALAH DR3, or RAVE DR6
ruwe		Gaia Renormalized Unit Weight Error
RAdeg	deg	R.A. (J2000)
DEdeg	deg	decl. (J2000)
GLON	deg	Galactic longitude
GLAT	deg	Galactic latitude
Uniq		whether unique, Y or N , priority: APOGEE > GALAH > RAVE
BinarySource		NaN, SED, APOGEE, GALAH, RAVE, Gaia, or the combinations

Note. Among the 1,566,810 entries in this catalog, there are 1,484,987 unique stars. The entire table is accessible online.

(This table is available in its entirety in machine-readable form.)

SB2 binary candidates found in our work (see Section 4 and Figure 10) and previously detected SB2/SB3 systems from the literature using APOGEE (Kounkel et al. 2021), GALAH (Traven et al. 2020), and RAVE (Matijevic et al. 2010) spectra.

For convenience, we also added Gaia DR3 binaries (`non-single_star=1` in table `gaiadr3.gaiasource`; Creevey et al. 2022) and Gaia EDR3 Renormalized Unit Weight Error (RUWE) values in Table 4. We note that while we listed

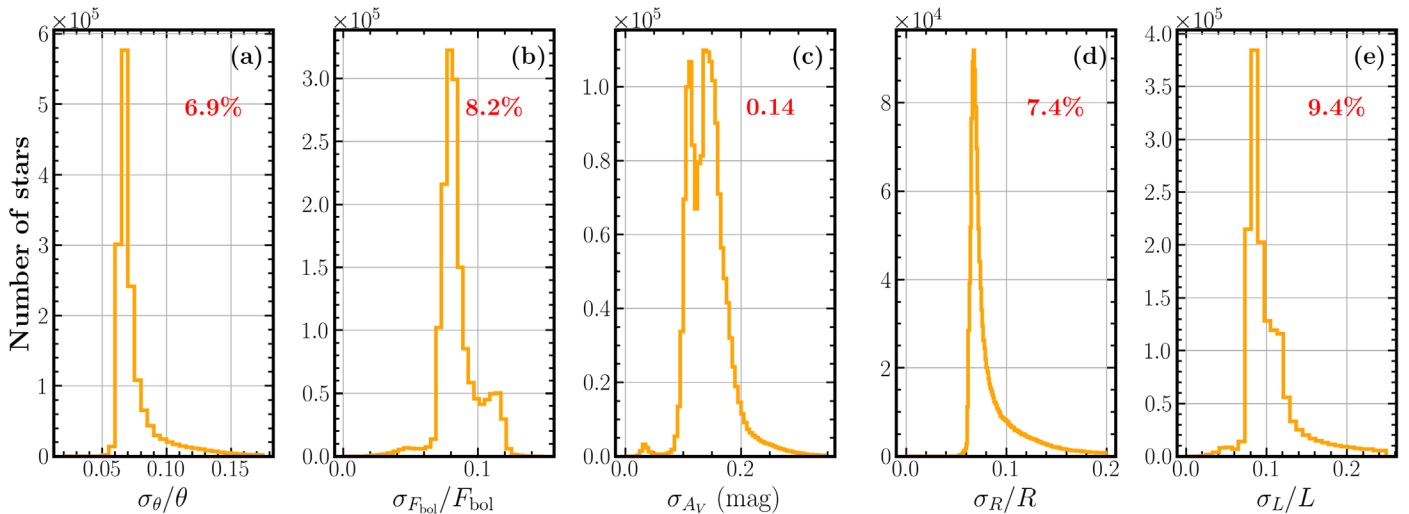


Figure 16. Uncertainty distributions of angular radius, bolometric flux, extinction, radius, and luminosity (from left to right). The numbers shown in red are the median uncertainties.

Gaia binaries, some binaries, such as SB1, should not significantly bias our SED fitting, as the fluxes of the primaries are not dramatically influenced by their companions. Second, our stellar parameter estimates for B stars, from APOGEE DR17, should be used with caution. This is because near-UV photometry is unavailable to constrain their SEDs.

6. Conclusions

We report revised stellar radii and extinctions for 1,484,498 unique stars in the low-to-high-extinction fields observed by the APOGEE, GALAH, and RAVE surveys (see Table 4 for data access). Specifically, we compare SEDs predicted by the widely used MARCS and BOSZ model spectra with 32 large-volume photometric bandpasses, combining data from nine major surveys: Gaia EDR3, 2MASS, ALLWISE, SkyMapper, Pan-STARRS, SDSS, APASS, Hipparcos, and Tycho2. Our careful compilation of the zero-points and transmission curves of these photometric systems, shown in Table 2, allows us to obtain high accuracy in the derived stellar parameter estimates. This work restricts the analysis to targets with available spectroscopy, as the availability of their spectroscopic T_{eff} estimates allows one to lift the temperature–extinction degeneracy.

The primary goals of this work are fourfold: (1) to design, validate, and demonstrate our publicly accessible pipeline, SEDEX,¹⁵ for carrying out SED fitting using data sets from massive surveys; (2) to provide stellar parameter estimates, such as radii and luminosities, which are critical, independent observational constraints for asteroseismic modeling with Kepler, TESS, and future PLATO data; (3) to provide a large sample of (36,854) SB2 MS binary candidates; and (4) to obtain interstellar extinctions and use them in our future work for constructing 3D dust maps for space-borne transit survey fields, such as the Kepler field, the TESS CVZs, and the PLATO LOPN and LOPS fields. This would be useful for deriving stellar parameters for asteroseismic analyses and exoplanet studies.

Our results are summarized below:

1. We homogenize cross-survey atmospheric parameters by calibrating GALAH and RAVE scales to those of APOGEE using neural networks. We also rescale the heterogeneous atmospheric parameter uncertainties (Section 2.2 and Table 1).
2. Our validation reports consistency with CHARA angular diameters ($3.07\% \pm 6.77\%$), HST CALSPEC bolometric flux ($3.41\% \pm 1.99\%$), and asteroseismic extinction (-0.039 ± 0.050), radius ($0.1\% \pm 4.9\%$), and luminosity ($-0.4\% \pm 4.2\%$) (Section 3).
3. We provide extinction estimates of the stars in APOGEE DR17, GALAH DR3, and RAVE DR6 data sets. Our extinction scale is in agreement with Green et al. (2019) at the $<1\%$ level but deviates from Queiroz et al. (2020) by $\sim 20\%$. The extinctions from our work and Green et al. (2019) produce color–magnitude diagrams that better match the MIST stellar evolutionary models.
4. We provide extinction values for 184 Gaia open clusters, each with at least three cluster members included in our sample. We then confirm the presence of differential extinction in NGC 6791 ($A_V = 0.18\text{--}0.63$ mag) and NGC 6819 ($A_V = 0.42\text{--}0.63$ mag) (Section 4.3). We obtain a global extinction value of $A_V = 0.41 \pm 0.19$ mag for NGC 6791 and $A_V = 0.53 \pm 0.16$ mag for NGC 6819.
5. Our catalog median precision is 6.9% for angular radius, 8.2% for bolometric flux, 0.14 mag for extinction, 7.4% for radius, and 9.4% for luminosity (Section 5). Note that we added in quadrature a 2.4% uncertainty floor to the T_{eff} uncertainties, which affects all of the uncertainty reported here.

Gaia Data Release 3 was released in 2022 June. Among other products, this catalog provides precise spectroscopic atmospheric parameters for ~ 5.6 million stars based on their high-resolution RVS spectra. Given that this data release does not comprise extinctions based on the high-resolution spectroscopic observations, in our next paper (J. Yu et al. 2023, in preparation) we will use the atmospheric parameters from this data release to infer precise stellar radii and derive a 3D extinction map. This map will cover the entire sky, beyond the current footprint of the APOGEE, GALAH, and RAVE

¹⁵ <https://github.com/Jieyu126/SEDEX>

surveys. Since this map covers several transit survey fields, such as the Kepler field, the TESS NCVZ and SCVZ, and the PLATO LOPN and LOPS fields, it will be useful for exoplanet studies and asteroseismic analysis.

Future Gaia Data Releases will enable the straightforward updates of stellar radii and luminosities to achieve better precision by combining Gaia distances with angular radii and bolometric fluxes retrieved from this work. The combination of these luminosity estimates with global seismic parameters will be valuable for deriving stellar ages for Galactic archeology (see the introduction). Our SEDEX pipeline can provide fundamental stellar parameters, which might be valuable to build stellar input catalogs for future missions, such as PLATO and Earth 2.0 (Ge et al. 2022).

We are greatly thankful for the referee's thorough review of the manuscript and helpful comments. We thank Nadiia Kostogryz, René Heller, Daniel Huber, Yuan-Sen Ting, Maosheng Xiang, and Haibo Yuan for discussions. J.Y. and L.G. acknowledge support from ERC Synergy grant WHOLE SUN 810218 and PLATO grants from the German Aerospace Center (DLR 50001501) and from the Max Planck Society. S. K. acknowledges support from the European Union's Horizon 2020 research and innovation program under grant agreement No. 101004110 and from the Netherlands Organisation for Scientific Research (NOVA). This work was funded by the Deutsche Forschungsgemeinschaft (DFG, German Research Foundation)—Project-ID 138713538—SFB 881 (“The Milky Way System,” subproject P02). S.H. acknowledges the ERC Consolidator grant DipolarSound (grant agreement No. 101000296). S.B. and J.Y. acknowledge the Joint Research Fund in Astronomy (U2031203) under a cooperative agreement between the National Natural Science Foundation of China (NSFC) and the Chinese Academy of Sciences (CAS).

ORCID iDs

Jie Yu  <https://orcid.org/0000-0002-0007-6211>
 Shourya Khanna  <https://orcid.org/0000-0002-2604-4277>
 Saskia Hekker  <https://orcid.org/0000-0002-1463-726X>
 Guillaume Dréau  <https://orcid.org/0000-0002-0135-8720>
 Laurent Gizon  <https://orcid.org/0000-0001-7696-8665>
 Shaolan Bi  <https://orcid.org/0000-0002-7642-7583>

References

- Abdurro'uf, Accetta, K., Aerts, C., et al. 2022, *ApJS*, 259, 35
 Aerts, C., Christensen-Dalsgaard, J., & Kurtz, D. W. 2010, *Asteroseismology* (Dordrecht: Springer)
 Aguirre, V. S., Bojsen-Hansen, M., Slumstrup, D., et al. 2018, *MNRAS*, 475, 5487
 Alam, S., Albareti, F. D., Prieto, C. A., et al. 2015, *ApJS*, 219, 12
 An, D., Terndrup, D. M., Pinsonneault, M. H., & Lee, J. 2015, *ApJ*, 811, 46
 Anders, F., Khalatyan, A., Queiroz, A. B. A., et al. 2022, *A&A*, 658, A91
 Andrae, R., Fousneau, M., Creevey, O., et al. 2018, *A&A*, 616, A8
 Bailer-Jones, C. A. L. 2011, *MNRAS*, 411, 435
 Bailer-Jones, C. A. L., Rybizki, J., Fousneau, M., Demleitner, M., & Andrae, R. 2021, *AJ*, 161, 147
 Baines, E. K., Dollinger, M. P., Cusano, F., et al. 2010, *ApJ*, 710, 1365
 Basu, S., & Chaplin, W. J. 2017, *Asteroseismic Data Analysis: Foundations and Techniques* (Princeton, NJ: Princeton Univ. Press)
 Berger, T. A., Huber, D., Gaidos, E., & van Saders, J. L. 2018, *ApJ*, 866, 99
 Berger, T. A., Huber, D., van Saders, J. L., et al. 2020, *AJ*, 159, 280
 Bessell, M., Bloxham, G., Schmidt, B., et al. 2011, *PASP*, 123, 789
 Bessell, M., & Murphy, S. 2012, *PASP*, 124, 140
 Bohlin, R. C., Gordon, K. D., & Tremblay, P. E. 2014, *PASP*, 126, 711
 Bohlin, R. C., Meszaros, S., Fleming, S. W., et al. 2017, *AJ*, 153, 234
 Borre, C. C., Aguirre Børsen-Koch, V., Helmi, A., et al. 2022, *MNRAS*, 514, 2527
 Borucki, W. J., Koch, D., Basri, G., et al. 2010, *Sci*, 327, 977
 Boyajian, T. S., von Braun, K., Feiden, G. A., et al. 2015, *MNRAS*, 447, 846
 Boyajian, T. S., von Braun, K., van Belle, G., et al. 2012, *ApJ*, 757, 112
 Boyajian, T. S., von Braun, K., van Belle, G., et al. 2013, *ApJ*, 771, 40
 Bragaglia, A., Carretta, E., Gratton, R. G., et al. 2001, *AJ*, 121, 327
 Brogaard, K., Arentoft, T., Jessen-Hansen, J., & Miglio, A. 2021, *MNRAS*, 507, 496
 Brogaard, K., VandenBerg, D. A., Bruntt, H., et al. 2012, *A&A*, 543, A106
 Buder, S., Sharma, S., Kos, J., et al. 2021, *MNRAS*, 506, 150
 Cantat-Gaudin, T., Anders, F., Castro-Ginard, A., et al. 2020, *A&A*, 640, A1
 Cardelli, J. A., Clayton, G. C., & Mathis, J. S. 1989, *ApJ*, 345, 245
 Casagrande, L., & VandenBerg, D. A. 2014, *MNRAS*, 444, 392
 Casagrande, L., & VandenBerg, D. A. 2018, *MNRAS*, 475, 5023
 Chambers, K. C., Magnier, E. A., Metcalfe, N., et al. 2016, arXiv:1612.05560
 Chaplin, W. J., & Miglio, A. 2013, *ARA&A*, 51, 353
 Chaplin, W. J., Serenelli, A. M., Miglio, A., et al. 2020, *NatAs*, 4, 382
 Choi, J., Dotter, A., Conroy, C., et al. 2016, *ApJ*, 823, 102
 Cohen, M., Wheaton, W. A., & Megeath, S. T. 2003, *AJ*, 126, 1090
 Creevey, O. L., Sordo, R., Pailler, F., et al. 2022, arXiv:2206.05864
 Cunha, M. S., Aerts, C., Christensen-Dalsgaard, J., et al. 2007, *A&ARv*, 14, 217
 Cutri, R. M., Skrutskie, M. F., van Dyk, S., et al. 2003, *yCat*, 2246
 Cutri, R. M., Wright, E. L., Conrow, T., et al. 2014, *yCat*, 2328
 Davenport, J. R. A., Ivezić, Ž., Becker, A. C., et al. 2014, *MNRAS*, 440, 3430
 Davies, G. R., Lund, M. N., Miglio, A., et al. 2017, *A&A*, 598, L4
 de Assis Peralta, R., Samadi, R., & Michel, E. 2018, *AN*, 339, 134
 De Silva, G. M., Freeman, K. C., Bland-Hawthorn, J., et al. 2015, *MNRAS*, 449, 2604
 D'Isanto, A., & Polsterer, K. L. 2018, *A&A*, 609, A111
 Donor, J., Frinchaoboy, P. M., Cunha, K., et al. 2020, *AJ*, 159, 199
 Dotter, A. 2016, *ApJS*, 222, 8
 Dréau, G., Mosser, B., Lebreton, Y., Gehan, C., & Kallinger, T. 2021, *A&A*, 650, A115
 Eastman, J. D., Rodriguez, J. E., Agol, E., et al. 2019, arXiv:1907.09480
 Feiden, G. A., & Chaboyer, B. 2012, *ApJ*, 757, 42
 Ferraro, F. R. 1992, *MmSAI*, 63, 491
 Fitzpatrick, E. L. 1999, *PASP*, 111, 63
 Fitzpatrick, E. L. 2004, in *ASP Conf. Ser. 309, Astrophysics of Dust*, ed. A. N. Witt, G. C. Clayton, & B. T. Draine (San Francisco, CA: ASP), 33
 Fitzpatrick, E. L., Massa, D., Gordon, K. D., Bohlin, R., & Clayton, G. C. 2019, *ApJ*, 886, 108
 Gaia Collaboration, Arenou, F., Babusiaux, C., et al. 2022, arXiv:2206.05595
 Gallart, C. 1998, *ApJL*, 495, L43
 Ge, J., Zhang, H., Zang, W., et al. 2022, arXiv:2206.06693
 Girardi, L., Bertelli, G., Bressan, A., et al. 2002, *A&A*, 391, 195
 Godoy-Rivera, D., Tayar, J., Pinsonneault, M. H., et al. 2021, *ApJ*, 915, 19
 Gordon, K. D., Fousneau, M., Arab, H., et al. 2016, *ApJ*, 826, 104
 Green, G. M., Schlafly, E., Zucker, C., Speagle, J. S., & Finkbeiner, D. 2019, *ApJ*, 887, 93
 Gustafsson, B., Edvardsson, B., Eriksson, K., et al. 2008, *A&A*, 486, 951
 Hall, O. J., Davies, G. R., Elsworth, Y. P., et al. 2019, *MNRAS*, 486, 3569
 Handberg, R., Brogaard, K., Miglio, A., et al. 2017, *MNRAS*, 472, 979
 Hardegree-Ullman, K. K., Zink, J. K., Christiansen, J. L., et al. 2020, *ApJS*, 247, 28
 Haykin, S. 1994, *Neural Networks: A Comprehensive Foundation* (Hoboken, NJ: Prentice Hall)
 Hekker, S., Angelou, G. C., Elsworth, Y., & Basu, S. 2020, *MNRAS*, 492, 540
 Hekker, S., & Christensen-Dalsgaard, J. 2017, *A&ARv*, 25, 1
 Heller, R., Harre, J., & Samadi, R. 2022, *A&A*, 665, A11
 Henden, A. A., Templeton, M., Terrell, D., et al. 2016, *yCat*, 2236
 Høg, E., Fabricius, C., Makarov, V. V., et al. 2000, *A&A*, 355, L27
 Hon, M., Huber, D., Kuzlewicz, J. S., et al. 2021, *ApJ*, 919, 131
 Howell, S. B., Sobeck, C., Haas, M., et al. 2014, *PASP*, 126, 398
 Huber, D., Basu, S., Beck, P., et al. 2019, *BAAS*, 51, 488
 Huber, D., Zinn, J., Bojsen-Hansen, M., et al. 2017, *ApJ*, 844, 102
 Husser, T.-O., Wende-von Berg, S., Dreizler, S., et al. 2013, *A&A*, 553, A6
 Jarrett, T. H., Cohen, M., Masci, F., et al. 2011, *ApJ*, 735, 112
 Jayasinghe, T., Kochanek, C. S., Stanek, K. Z., et al. 2021, *MNRAS*, 503, 200
 Jonsson, H., Holtzman, J. A., Prieto, C. A., et al. 2020, *AJ*, 160, 120
 Kane, S. R., Boyajian, T. S., Henry, G. W., et al. 2015, *ApJ*, 806, 60
 Karovicova, I., White, T. R., Nordlander, T., et al. 2020, *A&A*, 640, A25
 Karovicova, I., White, T. R., Nordlander, T., et al. 2022a, *A&A*, 658, A47
 Karovicova, I., White, T. R., Nordlander, T., et al. 2022b, *A&A*, 658, A48

- Khan, S., Miglio, A., Mosser, B., et al. 2019, *A&A*, **628**, A35
- Kharchenko, N. V., Piskunov, A. E., Schilbach, E., Roser, S., & Scholz, R.D. 2013, *A&A*, **558**, A53
- Kounkel, M., Covey, K. R., Stassun, K. G., et al. 2021, *AJ*, **162**, 184
- Kraus, A. L., Tucker, R. A., Thompson, M. I., Craine, E. R., & Hillenbrand, L. A. 2011, *ApJ*, **728**, 48
- Kurucz, R. L. 1979, *ApJS*, **40**, 1
- Lebreton, Y., & Goupil, M. J. 2014, *A&A*, **569**, A21
- Ligi, R., Creevey, O., Mourard, D., et al. 2016, *A&A*, **586**, A94
- Lindgren, L., Klioner, S. A., Hernandez, J., et al. 2021, *A&A*, **649**, A2
- Maestro, V., Che, X., Huber, D., et al. 2013, *MNRAS*, **434**, 1321
- Maíz Apellániz, J., Evans, C. J., Barba, R. H., et al. 2014, *A&A*, **564**, A63
- Mann, A. W., Feiden, G. A., Gaidos, E., Boyajian, T., & Braun, K. v. 2015, *ApJ*, **804**, 64
- Mann, A. W., & von Braun, K. 2015, *PASP*, **127**, 102
- Marrese, P. M., Marinoni, S., Fabrizio, M., & Altavilla, G. 2019, *A&A*, **621**, A144
- Matijevic, G., Zwitter, T., Munari, U., et al. 2010, *AJ*, **140**, 184
- McDonald, I., Zijlstra, A. A., & Boyer, M. L. 2012, *MNRAS*, **427**, 343
- McDonald, I., Zijlstra, A. A., & Watson, R. A. 2017, *MNRAS*, **471**, 770
- Miglio, A., Chiappini, C., Mackereth, J. T., et al. 2021, *A&A*, **645**, A85
- Mints, A., & Hekker, S. 2017, *A&A*, **604**, A108
- Mints, A., & Hekker, S. 2018, *A&A*, **618**, A54
- Nascimbeni, V., Piotto, G., Borner, A., et al. 2022, *A&A*, **658**, A31
- O'Donnell, J. E. 1994, *ApJ*, **422**, 158
- Onken, C. A., Wolf, C., Bessell, M. S., et al. 2019, *PASA*, **36**, e033
- Pinsonneault, M. H., Elsworth, Y. P., Tayar, J., et al. 2018, *ApJS*, **239**, 32
- Platais, I., Gosnell, N. M., Meibom, S., et al. 2013, *AJ*, **146**, 43
- Queiroz, A. B. A., Anders, F., Chiappini, C., et al. 2020, *A&A*, **638**, A76
- Rabus, M., Lachaume, R., Jordan, A., et al. 2019, *MNRAS*, **484**, 2674
- Rauer, H., Catala, C., Aerts, C., et al. 2014, *ExA*, **38**, 249
- Recio-Blanco, A., de Laverny, P., Palicio, P. A., et al. 2022, arXiv:2206.05541
- Ricker, G. R., Winn, J. N., Vanderspek, R., et al. 2015, *JATIS*, **1**, 014003
- Riello, M., De Angeli, F., Evans, D. W., et al. 2021, *A&A*, **649**, A3
- Rosvick, J. M., & VandenBerg, D. A. 1998, *AJ*, **115**, 1516
- Serenelli, A., Johnson, J., Huber, D., et al. 2017, *ApJS*, **233**, 23
- Silva Aguirre, V., Lund, M. N., Antia, H. M., et al. 2017, *ApJ*, **835**, 173
- Spada, F., Demarque, P., Kim, Y.-C., & Sills, A. 2013, *ApJ*, **776**, 87
- Spina, L., Ting, Y., De Silva, G. M., et al. 2021, *MNRAS*, **503**, 3279
- Steinmetz, M., Guiglion, G., McMillan, P. J., et al. 2020a, *AJ*, **160**, 83
- Steinmetz, M., Matijević, G., Enke, H., et al. 2020b, *AJ*, **160**, 82
- Stello, D., Saunders, N., Grunblatt, S., et al. 2022, *MNRAS*, **512**, 1677
- Tayar, J., Clayton, Z. R., Huber, D., & van Saders, J. 2022, *ApJ*, **927**, 31
- ten Brummelaar, T. A., McAlister, H. A., Ridgway, S. T., et al. 2005, *ApJ*, **628**, 453
- Ting, Y., Hawkins, K., & Rix, H. 2018, *ApJL*, **858**, L7
- Tonry, J. L., Stubbs, C. W., Lykke, K. R., et al. 2012, *ApJ*, **750**, 99
- Traven, G., Feltzing, S., Merle, T., et al. 2020, *A&A*, **638**, A145
- van Leeuwen, F. 2007, *A&A*, **474**, 653
- Vines, J. I., & Jenkins, J. S. 2022, *MNRAS*, **513**, 2719
- von Braun, K., Boyajian, T. S., van Belle, G. T., et al. 2014, *MNRAS*, **438**, 2413
- White, T. R., Huber, D., Mann, A. W., et al. 2018, *MNRAS*, **477**, 4403
- Wilson, J. C., Hearty, F. R., Skrutskie, M. F., et al. 2019, *PASP*, **131**, 055001
- Wu, T., Li, Y., & Hekker, S. 2014, *ApJ*, **786**, 10
- Yu, J., Hekker, S., Bedding, T. R., et al. 2021, *MNRAS*, **501**, 5135
- Yu, J., Huber, D., Bedding, T. R., et al. 2018, *ApJS*, **236**, 42
- Zinn, J. C. 2021, *AJ*, **161**, 214
- Zinn, J. C., Pinsonneault, M. H., Huber, D., & Stello, D. 2019, *ApJ*, **878**, 136
- Zinn, J. C., Stello, D., Elsworth, Y., et al. 2022, *ApJ*, **926**, 191